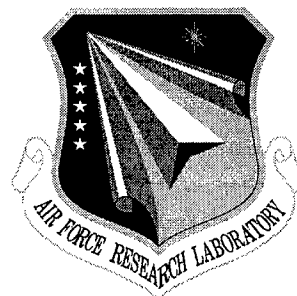AFRL-SN-RS-TR-1999-42
Final Technical Report
March 1999

# INTEGRATED LASER MODULE

Cornell University

J. M. Ballantyne

*APPROVED FOR PUBLIC RELEASE; DISTRIBUTION UNLIMITED.*

19990504 071

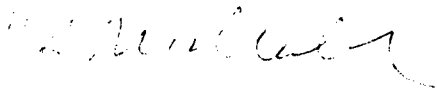**AIR FORCE RESEARCH LABORATORY
SENSORS DIRECTORATE
ROME RESEARCH SITE
ROME, NEW YORK**

DTIC QUALITY INSPECTED 4

This report has been reviewed by the Air Force Research Laboratory, Information Directorate, Public Affairs Office (IFOIPA) and is releasable to the National Technical Information Service (NTIS). At NTIS it will be releasable to the general public, including foreign nations.
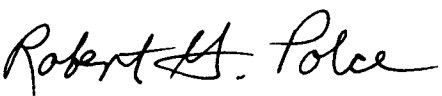
AFRL-SN-RS-TR-1999-42 has been reviewed and is approved for publication.

APPROVED:

RICHARD J. MICHALAK
Project Engineer

FOR THE DIRECTOR:

ROBERT G. POLCE, Acting Chief
Rome Operations Office
Sensors Directorate

If your address has changed or if you wish to be removed from the Air Force Research Laboratory Rome Research Site mailing list, or if the addressee is no longer employed by your organization, please notify AFRL/SNDR, 25 Electronic Parkway, Rome, NY 13441-4515.. This will assist us in maintaining a current mailing list.

Do not return copies of this report unless contractual obligations or notices on a specific document require that it be returned.

# REPORT DOCUMENTATION PAGE

Public reporting burden for this collection of information is estimated to average 1 hour per response, including the time for reviewing instructions, searching existing data sources, gathering and maintaining the data needed, and completing and reviewing the collection of information. Send comments regarding this burden estimate or any other aspect of this collection of information, including suggestions for reducing this burden, to Washington Headquarters Services, Directorate for Information Operations and Reports, 1215 Jefferson Davis Highway, Suite 1204, Arlington, VA 22202-4302, and to the Office of Management and Budget, Paperwork Reduction Project (0704-0188), Washington, DC 20503.

| 1. AGENCY USE ONLY (Leave blank) | 2. REPORT DATE | 3. REPORT TYPE AND DATES COVERED | |
|---|---|---|---|
| | March 1999 | Final    Aug 95 - Jul 98 | |

**4. TITLE AND SUBTITLE**

INTEGRATED LASER MODULE

**5. FUNDING NUMBERS**
C - F30602-95-1-0041
PE - 63726F
PR - 2863
TA - 92
WU - 76

**6. AUTHOR(S)**

J. M. Ballantyne

**7. PERFORMING ORGANIZATION NAME(S) AND ADDRESS(ES)**

Cornell University
Office of Sponsored Programs
120 Day Hall
Ithaca NY 14853-2801

**8. PERFORMING ORGANIZATION REPORT NUMBER**

N/A

**9. SPONSORING/MONITORING AGENCY NAME(S) AND ADDRESS(ES)**

Air Force Research Laboratory/SNDR
25 Electronic Parkway
Rome NY 13441-4515

**10. SPONSORING/MONITORING AGENCY REPORT NUMBER**

AFRL-SN-RS-TR-1999-42

**11. SUPPLEMENTARY NOTES**

Air Force Research Laboratory Project Engineer: Richard J. Michalak/SNDR/(315) 330-3150

**12a. DISTRIBUTION AVAILABILITY STATEMENT**

Approved for public release; distribution unlimited

**12b. DISTRIBUTION CODE**

**13. ABSTRACT** (Maximum 200 words)

This program developed waveguide diode ring lasers (WDRLs) for incorporation onto laser modules for applications in data transmission requiring low noise, single mode sources which can be incorporated as arrays into small, inexpensive modules with moderate output powers. Capabilities of WDRLs developed in this program include wavelengths at 1.3 micron and shorter, 30 db side-mode-suppression ratios, tens of milliwatts of output power, relative intensity noise of -150 dbm, threshold current down to 5 mA, direct modulation bandwidth of 9 GHz, electrically-switched beam steering, highly integrable and low-cost manufacturability based on etch-defined optical cavities and planar processing technologies which do not require regrowth, and monolithic integration of lasers, detectors and amplifiers. The key concepts enabling this performance are protected under two patents. Techniques for passive alignment of 12-laser arrays to single mode fiber ribbon were developed. Materials for monolithic lasers on Si were developed which showed stimulated emission and should enable cheap, passive alignment of large laser arrays with single mode fibers.

**14. SUBJECT TERMS**

Laser Modules, Ring Laser, Waveguide Modeling, Laser Packaging

**15. NUMBER OF PAGES**
64

**16. PRICE CODE**

| 17. SECURITY CLASSIFICATION OF REPORT | 18. SECURITY CLASSIFICATION OF THIS PAGE | 19. SECURITY CLASSIFICATION OF ABSTRACT | 20. LIMITATION OF ABSTRACT |
|---|---|---|---|
| UNCLASSIFIED | UNCLASSIFIED | UNCLASSIFIED | UL |

# Index

# Diode Ring Lasers for Modules

## I. Introduction (*)

As their complexity continues to increase, the performance of modern information systems is increasingly limited by data transmission within the system, rather than by the speed of the transistors doing the processing. This is true of the interconnects at the chip level, as well as intrachip, board, backplane, local area net and long distance transmission. As data rates and system complexity increase, individual components become smaller and more tightly packed, the power required to send the data increases, problems of cross talk and noise become more severe, manufacturing yield and reliability decrease and the interconnect limits all aspects of system performance and cost.

Many of these problems can be eliminated or reduced by using photons, instead of electrons, to transfer data from one point to another within the system. A characteristic of complex systems is that the number of interconnects required increases as one progresses to the smallest distances in the system. Hence one characteristic of applications for short distance optical interconnects is the highly parallel nature of the interconnects which requires many transmitters and receivers. Therefore, one of the most significant problems is the conversion of electrical to optical signals in a way which is efficient and compatible with silicon chip technology in terms of manufacturability, cost per function, size, reliability, and power density. Thus the cost, size, and performance of laser source modules are major hindrances to the more widespread use of optical data links at short to intermediate distances for transmission of large dynamic range signals at millimeter-wave bandwidths, and for high speed digital data. Traditional approaches using high performance DFB semiconductor lasers, diode-pumped solid state lasers, or the newer VCSEL semiconductor laser, each suffer some combination of cost, complexity, size, or performance limitations.

For example, although they show low noise and small size, the grating fabrication and regrowth associated with DFB lasers makes them very expensive (of order of $10^4$ each) and output powers are usually 10 mW or less. Diode-pumped solid state lasers are also expensive, much bulkier and less efficient that semiconductor lasers and as a consequence are totally unsuitable for array and large numbers applications, although they have high spectral purity and low noise. VCSELs are easily integrable, power efficient, and are very small. They require a very complex layer structure which may not be manufacturable at very low cost; their noise properties are not well studied yet, but should be good for single radial mode devices. The most serious limitation of VCSELs may be the difficulty of coupling substantial amounts of optical power to small, single mode waveguides, and having output perpendicular to the wafer surface, they may be difficult to monolithically integrate with other optical devices, such as modulators or amplifiers.

In recent years some work has been devoted in a number of laboratories to the development of monolithic diode ring lasers. Such devices have been developed in circular [1], oval [2], square [3], and triangular geometries [4], and some have shown single mode and unidirectional operation [2, 5]. See Figure 1.

(*) — This section is abstracted from the original proposal on Integrated Laser Modules, dated July 1995.
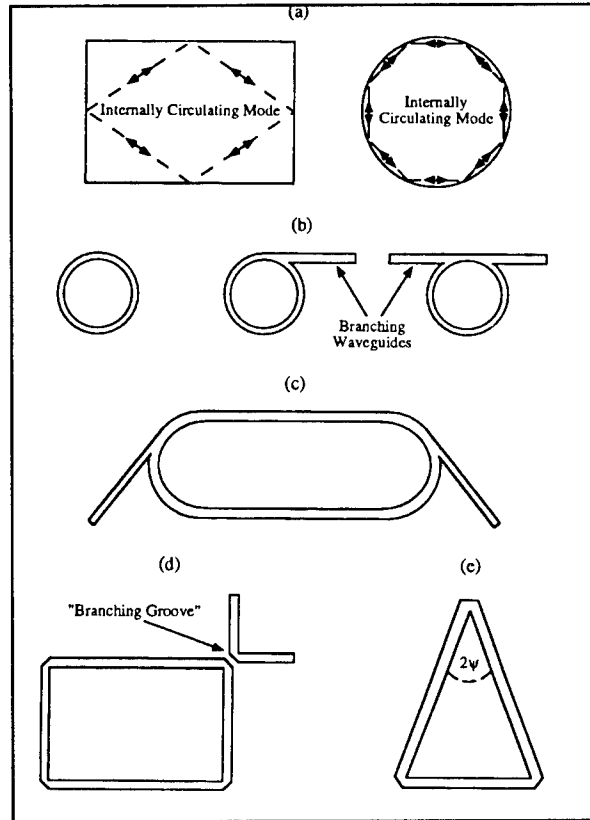
**Figure 1:** *Different semiconductor ring laser geometries. (A) Internally operating ring laser mode of structure with 4-cleaved sides6 or "whispering gallery" mode of microdisk and pillbox type lasers [7]. (B) Circular ring geometry with one or two branching waveguides for output coupling [8, 1]. C) Racetrack geometry with branching waveguides [2]. (D) Rectangular ring geometry with "branching groove" for output coupling [3]. (E) Triangular ring geometry [9, 10].*
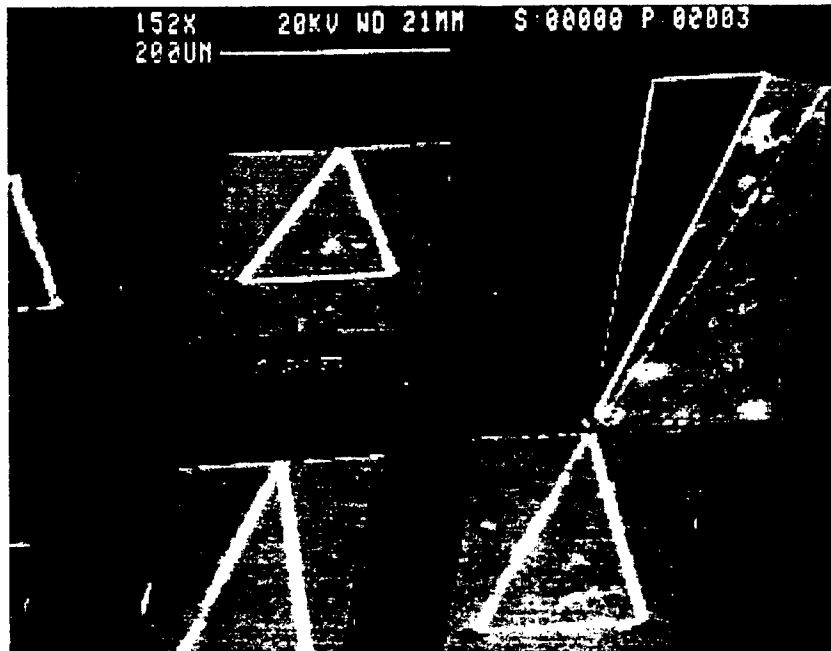


**Figure 2:** *SEM of an amplifier integrated with a ring laser.*

Diode ring lasers have also been monolithically integrated with waveguides and amplifiers [10, 11], and the theoretical understanding of these structures has seen significant advances [12, 13]. An SEM image of an integrated WDRL and amplifier is shown in Figure 2.

Devices in the triangular geometry have shown a unique combination of high output power (85 mW), single mode operation with high sidemode suppression ratios (> 25 dB), unidirectional operation, low threshold unbonded CW operation (14 mA) and all-etched, low cost, reproducible, manufacturable process technology [10]. The ability of these devices to simultaneously satisfy the requirements of high optical performance (low noise, high power), small size, and very low cost is unique among diode ring lasers and other planar diode lasers.

An important feature of WDRLs is their ability to operate in a pure traveling-wave, unidirectional mode. No other semiconductor laser possesses this property, which is very important for noise considerations, for improving output power, and for dealing with reflected light from the rest of the optical system. To operate unidirectionally, asymmetric forward or backward coupling must be present [14]. An example of one realization is shown in Figure 3.
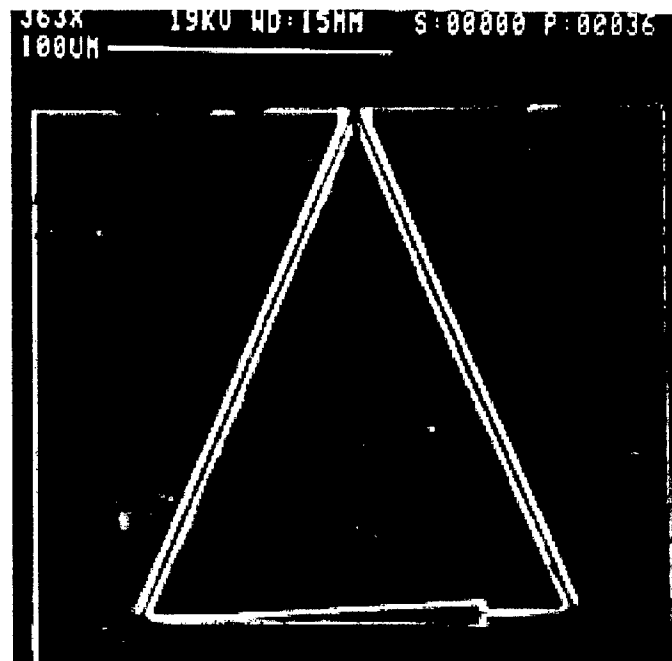


*Figure 3: SEM of a ring laser with an optical diode.*

The diode structure presents different back reflections for the two senses of circulation around the ring, forcing the laser to operate in the direction of the diode, as predicted [14]. The ratio of beam powers in clockwise to counterclockwise direction is 20:1. The process of enforcing unidirectionality is efficient, as shown in Figures 4 and 5.

3
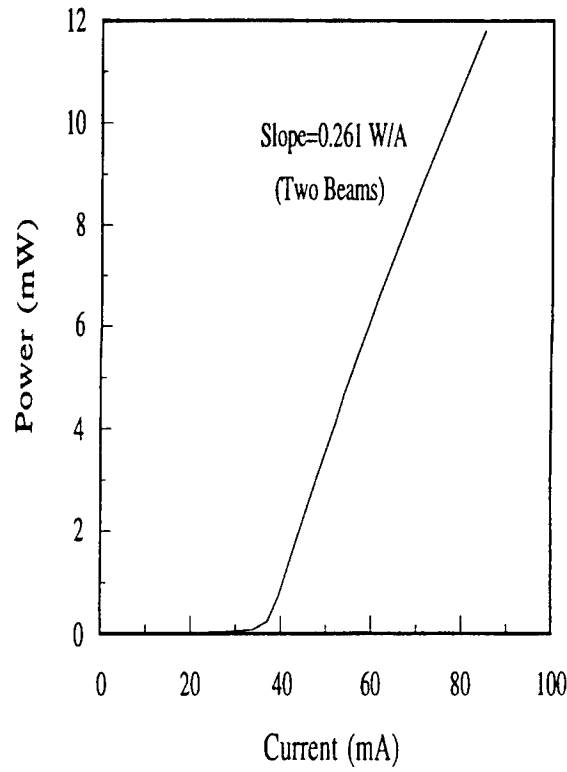
**Figure 4:** *Pulsed light-current characteristics of a standard ring laser, with the power being the combined output from the two beams. The ring cavity length is 800 μm, the ridge width is 4 μm, and the structure angle is 10° (#4135).*
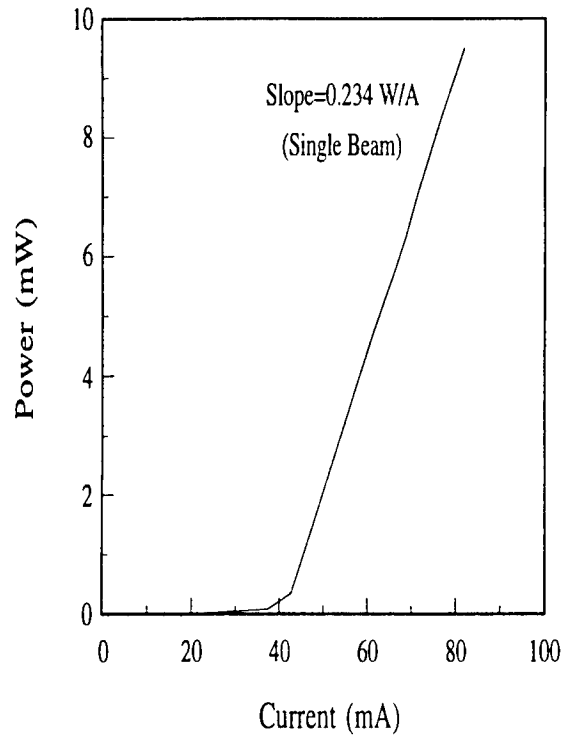


**Figure 5:** *Pulsed single-beam light-current characteristics of a ring laser with an optical diode. The ring cavity length is 800 μm, the ridge width is 4 μm, and the structure angle is 12° (#4137).*

There it is seen that the threshold current increases from about 38.5 to 41 mA when the diode is incorporated, a change of about 6% due to the loss of the diode structure, but the single beam external slope efficiency increases 78%. (For the ideal case the threshold current would not change, but the slope efficiency would double.) The consequences on the spectrum are quite remarkable, as shown in Figure 6. The ring lasers are much more single mode than the equivalent Fabry-Perot device. Bidirectional rings typically show 10 dB increase in side-mode suppression ratio over Fabry-Perot lasers, and unidirectional rings show an additional 7 - 10 dB increase over bidirectional rings.
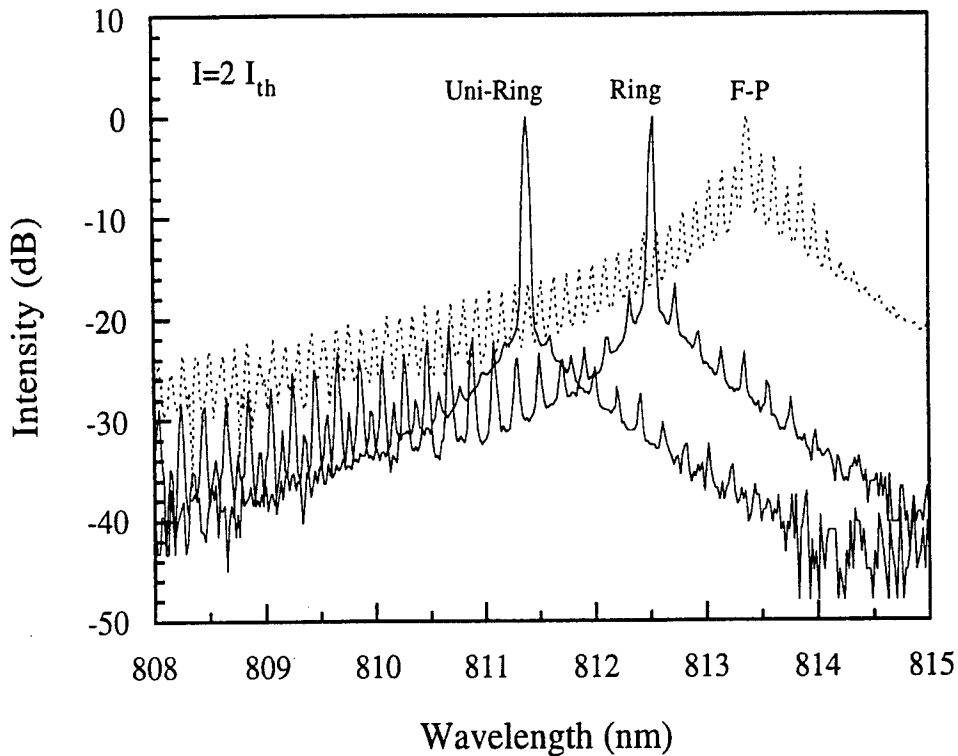


*Figure 6: CW log-spectra of a unidirectional ring laser (800 μm) with an optical diode (#4137, $I_{th}$=42 mA), a standard ring laser (800 μm) (#4135, $I_{th}$=38 mA), and a Fabry-Perot laser (700 μm) (#4107, $I_{th}$=32 mA), with each biased at twice its threshold current.*

This has a direct consequence on noise improvement. A side-mode suppression ratio (SMSR) of at least 17 dB at bias is required to make mode-partition noise negligible. Our unidirectional WDRLs show SMSR's exceeding 25 dB - meaning the side modes are nearly an order of magnitude smaller than required. No other semiconductor laser, except for very high quality DFB, exceeds this value. Furthermore, the optical diodes have yet to be optimized and the unidirectionality is only 20:1, so there is still ample room for the improvements we will make in the course of our module development.

In summary, waveguide diode ring lasers (WDRL) offer a new approach to simultaneously satisfy requirements for high power and low noise optical performance, together with very low cost and small physical size laser source modules for applications in optical data links at short to medium distances for transmission of large dynamic range, mm bandwidth, or digital signals. The demonstrated performance, understanding, and fabrication technology for WDRLs are now at the

level where their application and packaging in source modules should be undertaken. Preliminary packaging and materials work now holds out the promise for some very unique, almost revolutionary solutions to the low-cost packaging problem as well. We therefore propose a 3-year program to develop a prototype WDRL laser source module, to develop the capabilities of WDRLs to meet the wavelength, noise and power requirements of short distance optical links for large dynamic range, m-m wave signals, and to begin exploration of a new packaging and materials paradigm.

The following sections summarize the accomplishments and progress made under this program. Due to major reorganization in the Air Force, funding for this work was truncated after two years, causing the workforce to be reduced by more than 50% (5 personnel laid off) and termination of much ongoing work. Nevertheless, major accomplishments were made in improving devices and materials, and in meeting many of the original goals.

## II.    Accomplishments

## II.1   WDRL Device Development

### II.1.1  Low Threshold, Low Noise Devices

In this program, Mr. Booth has been engaged in process development to optimize triangular ring lasers for low threshold current, and for high asymmetry between the clockwise and counterclockwise-circulating power. He has been using a high quality d-doped InGaAs-quantum-well material with a very low transparency current density, which allows us to make especially low threshold ring lasers. Processing this material has proved to be difficult, however, because the topmost epitaxial layers seem to be exceptionally prone to damage when exposed to RIE during processing. This damage produces high contact resistance and poor current distribution across the lasers. For this reason, the first devices we made failed to operate except at very high drive currents. Our first solution to this problem was to apply the metal p-contact as the first step in the process, and then use that metal as the etch mask for the mirrors and ridge waveguides. We developed an efficient recipe, incorporating a chrome etch mask, which allowed us to use one etch step for both mirrors and ridges. However, due to the roughness of the chrome-masked mirrors and the difficulty of obtaining good electrical contact through the chrome (the surface of which tends to oxidize in air), we decided to return to $SiO_2$ etch masks. In our newest process, the p-contact metal is applied in the first step to protect the underlying semiconductor surface, but then the metal is covered over with PECVD $SiO_2$, which is patterned and used as the etch mask for the laser structure.

By refining the ring laser fabrication process, we have produced a triangular ring laser with the smallest threshold current measured to date (5 mA). This value remains larger than the predicted limit of 2 mA. Figure 7 shows the theoretically attainable threshold currents, which are derived by combining measured material parameters with the theoretically calculated reflectivity of the turning mirrors.
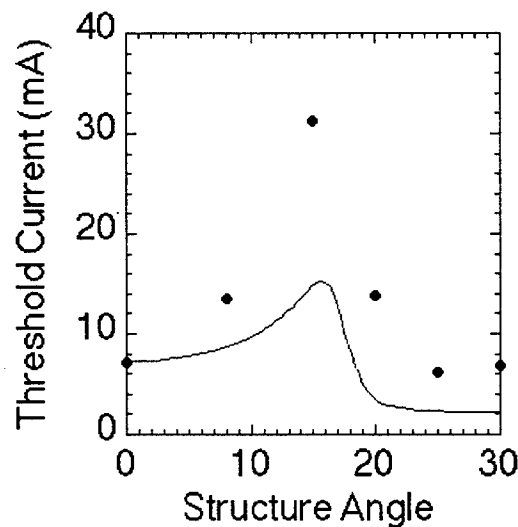
*Figure 7: Solid curve: Threshold current of an optimum-length device as a function of structure angle. Points: lowest threshold current observed in actual devices. At each angle, devices with a range of lengths were tested, and the smallest threshold current found is shown here.*

The figure also shows the smallest threshold currents obtained to date. Although the theory predicts turning mirror reflectivities of up to 90%, and such values have been obtained in previous fabrication runs, we find that our most recent devices have effective reflectivities of only 70%. A likely explanation for this is the existence of leakage currents. For example, the new ring laser process leaves material at the edge of each mirror, and this provides a path for parasitic current flow. These regions can be seen to glow when the laser is energized, which provides direct evidence that unwanted currents are flowing through them. Also, while the etched mirrors are of relatively high quality, there is still some residual scattering loss due to mirror surface roughness.

Our devices show a new and unexpected behavior: bistable switching between two different output directions. Figure 8 shows two infrared photos of a ring laser driven well above threshold. The output beams from the laser are partially scattered from the semiconductor surface, and so are visible in the photos.
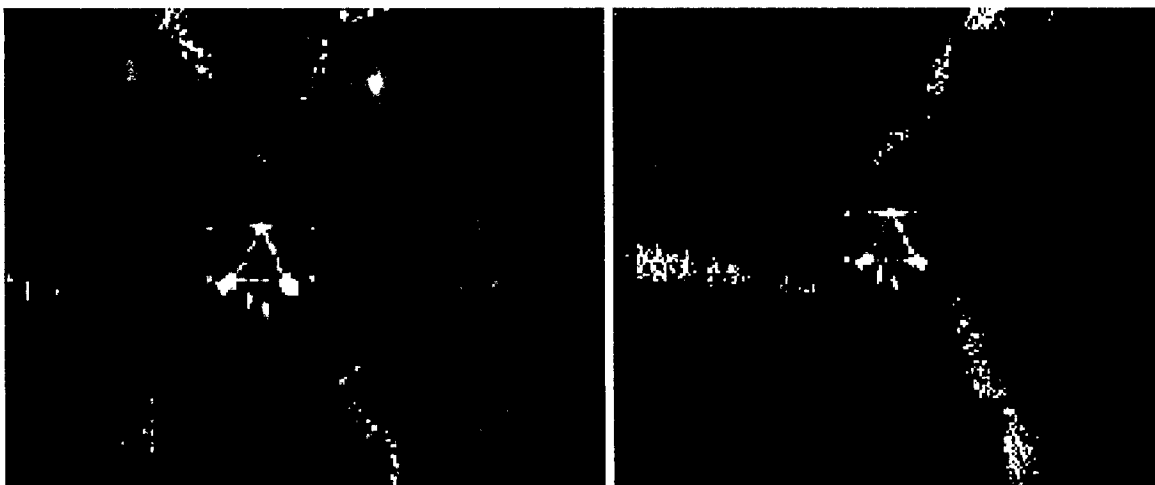


*Figure 8: Infrared camera photos of a ring laser (length 400 μm, structure angle 25°) driven at 22 mA (left side) and 38 mA (right side). At the higher drive current, the laser operates unidirectionally.*

At the lower drive current we see two beams from each mirror, corresponding to the clockwise (CW) and counterclockwise (CCW) circulating beams, but as the current is increased the device suddenly switches to a unidirectional CW mode. Three of the beams disappear, and the remaining three double in intensity, as shown on the right side of Figure 8. This behavior has been seen in devices with a variety of different lengths, structure angles, and quantum-well material structures.

To further illustrate that these ring lasers are bistable devices, the light-current curves for the CW and CCW beams of a ring laser are shown in Figure 9.

As the current is increased the CW power is slightly dominant, but at 100 mA the CCW power triples while the CW power drops almost to the spontaneous emission level. After this switch the CCW/CW power ratio is as large as 45 to 1 – the largest ratio of circulating powers ever observed for a triangular ring laser. The two states of the laser exhibit large hysteresis: once switched on, the unidirectional mode remains stable until the current is reduced below 60 mA. We suspect that this bistability is caused by gain competition between the two circulating modes.

The bistable devices have been used to confirm the hypothesis that a unidirectional ring laser should have smaller output power fluctuations than a bidirectional one, because of the reduction in partition noise between the two circulating modes.
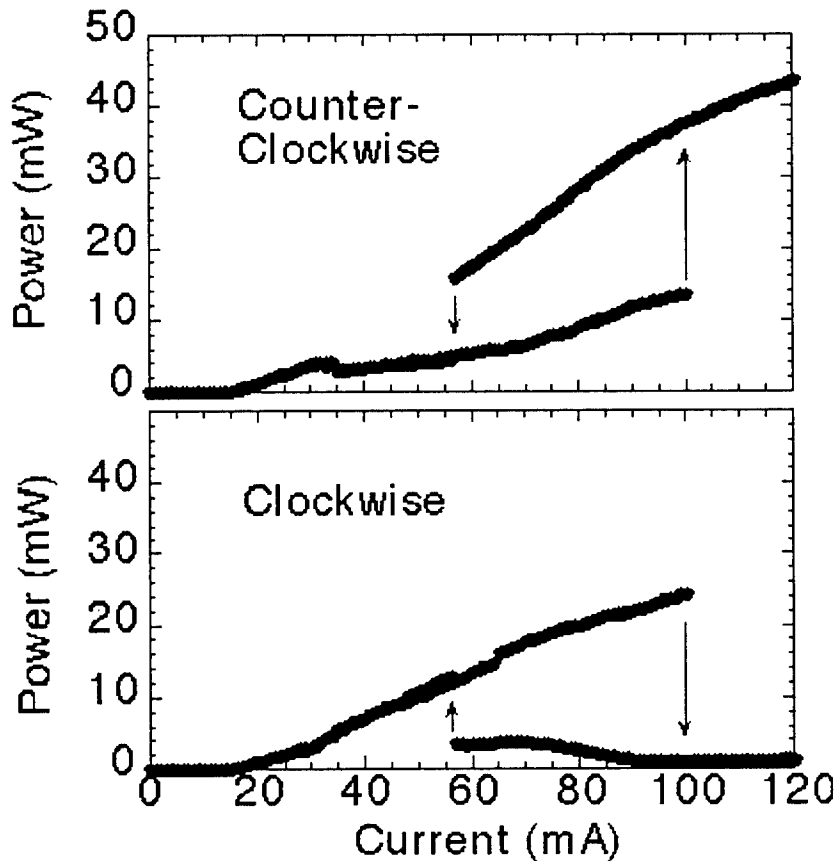


*Figure 9: L-I curves for a triangular ring laser with structure angle of 8° and length of 600 µm. Note: This device is emitting 40mW into a single mode with -150 dbm RIN*
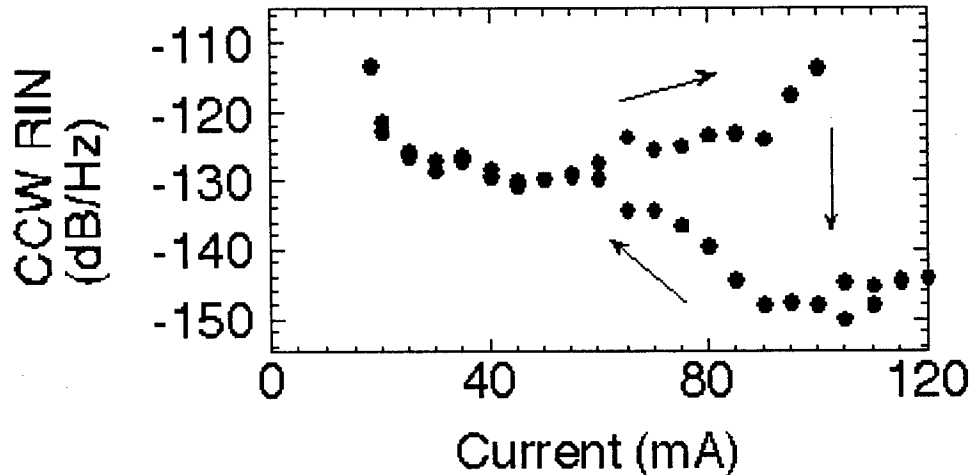
**Figure 10:** *Relative intensity noise as a function of current, plotted for the counter-clockwise circulating beam from the device of Figure 9.*

Figure 10 shows the relative intensity noise (RIN) of the CCW beam from the device of Figure 9. As the drive current increases, the RIN remains relatively large (-120 to -130 dB/Hz), but when the device is driven to 100 mA and switches to the unidirectional mode the RIN suddenly drops to -150 dB/Hz. Then, as the drive current is decreased again, the RIN gradually climbs back to its former value.

## II.1.2, 1.3 μm Wavelength Devices

### Process Development

The long wavelength triangular ring laser is fabricated in a triple quantum well epitaxial material with InGaAsP active region, 2 μm thick InP cladding layers on either side and 0.25 μm InGaAs cap. A self aligned process is used to precisely define the 4 μm wide ridge and facets using a single $SiO_2$ mask. The ridge and facets are etched to different depth in two different etches, producing a single lateral mode ridge waveguide structure. Key processing development issues include developing a dry etching recipe for fabricating smooth and vertical laser mirrors in the InP/InGaAsP material system with moderate etch speed for accurate etch depth control. Dry etching of InP containing material is very difficult due to the low volatility of InP and In containing compound, which tends to micromask and produce surface roughness. Furthermore, an etch masking material must be found with sufficiently high selectivity to InP/InGaAsP, and easily removed without affecting the $SiO_2$ etch mask covering other regions of the device. Wet chemical, RIBE and ECR etching, regular and UV cured photoresist as etch masks were examined and rejected during the process development. Eventually, a high temperature (200 °C), low pressure ($<10^{-4}$ torr), high voltage (1000V) CAIBE etching recipe is developed that produces smooth and vertical facets with surface roughness less than 400Å, etch rates at 0.3 μm/min. PECVD amorphous carbon is found as a good dielectric etch mask with approximately 25:1 selectivity. The amorphous carbon can be easily removed after the etch in oxygen plasma without affecting the $SiO_2$ masks, making it compatible with the rest of the process.

## General Device Characterization

Triangular ring lasers and FPs were fabricated on the same chip using the above-mentioned process. SEM picture of a fabricated ring laser is shown in Figure 11.
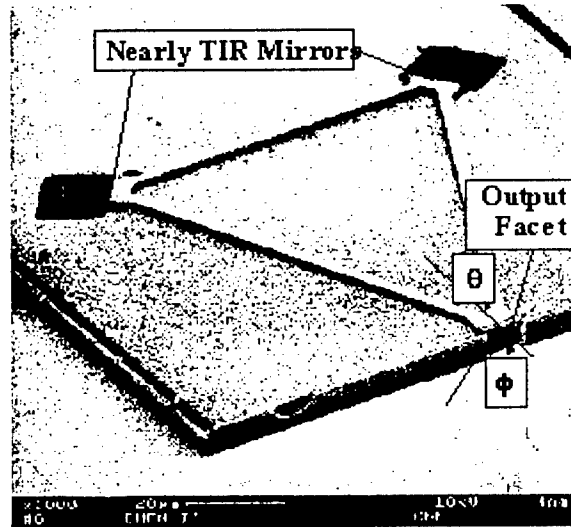


*Figure 11:* Fabricated 1.3 µm triangular ring laser.

The devices were pulse tested at room temperature, and CW tested with the sample lapped and bonded onto a Cu heatsink and cooled to -30°C stage temperature. Due to the relatively low differential gain of the material (1.6 kA/cm$^2$ for 500 µm Broad Area cleaved facet FP), the threshold currents of these particular devices are fairly high, ranging between 100 to 250 mA. Much better material has been demonstrated, so this is not an inherent limitation of 1.3 µm WDRLs. The unpackaged devices were able to operate pulsed at room temperature and CW close to 0° C with heatsink. General device characteristics, such as PI, optical spectrum, farfield were measured, and found to correlate well with theoretical predictions. The Ring lasers demonstrated higher SMSR than FP lasers on the same chip, confirming the previous works in the short wavelength GaAs/AlGaAs material. The best ring laser (Figure 12) demonstrated SMSR up to 30dB, and remaining single mode up to three times the threshold current.
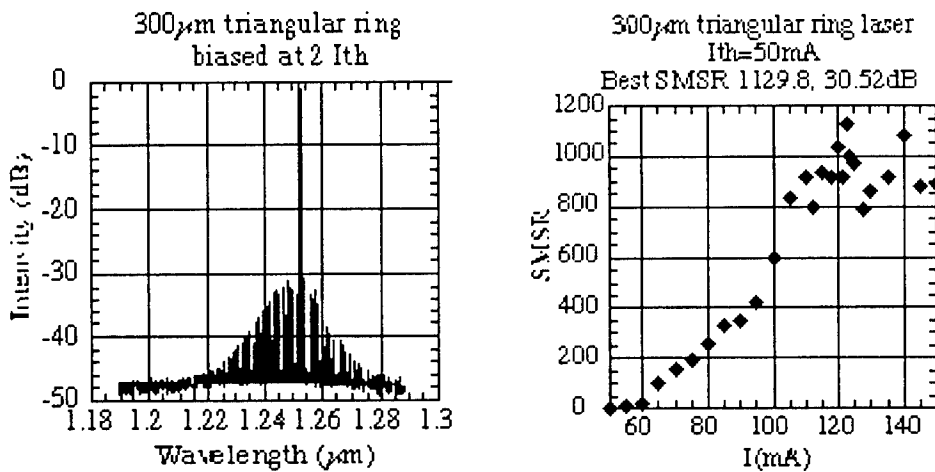


*Figure 12:* Spectrum and SMSR vs I for 300µm ring laser.

## Intensity Noise Measurements

The Relative Intensity Noise (RIN) of the semiconductor ring lasers was measured using a HP7100C Lightwave Signal Analyzer system. System thermal noise and photon shot noise were subtracted from the measured RIN, to arrive at the true laser RIN. The devices were CW operated at -30°C, and the output was coupled into a single mode fiber using a custom designed coupling setup. (Figure 13).
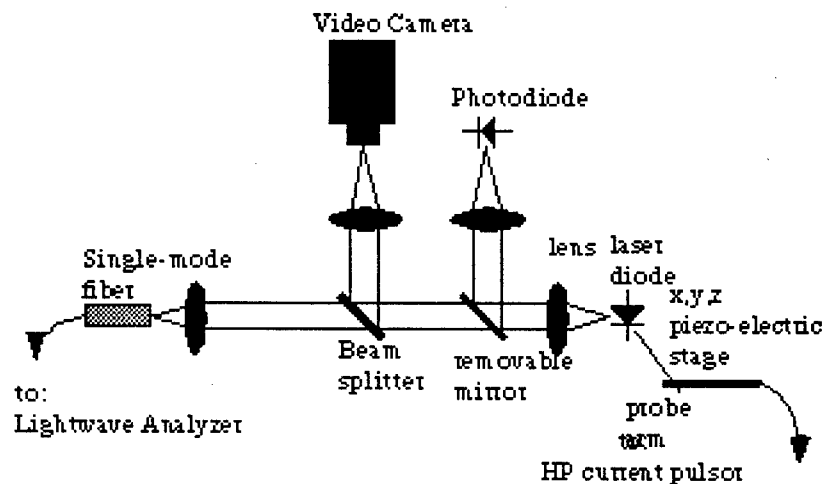


*Figure 13:* Relative Intensity Noise measurement setup.

The laser output was collimated, then focused into the single mode fiber using a microscope objective. The signal was then coupled into the Lightwave Analyzer. The coupling efficiency into the single mode fiber is around 30% relative to the input of the focusing objective. The ring lasers are very sensitive to weak feedback from the single mode fiber front surface, requiring the insertion of a 30 dB isolator. Periodic external cavity modes are observed, while the entire noise level are raised without the isolator, showing signs of coherence collapse (Figure 14).
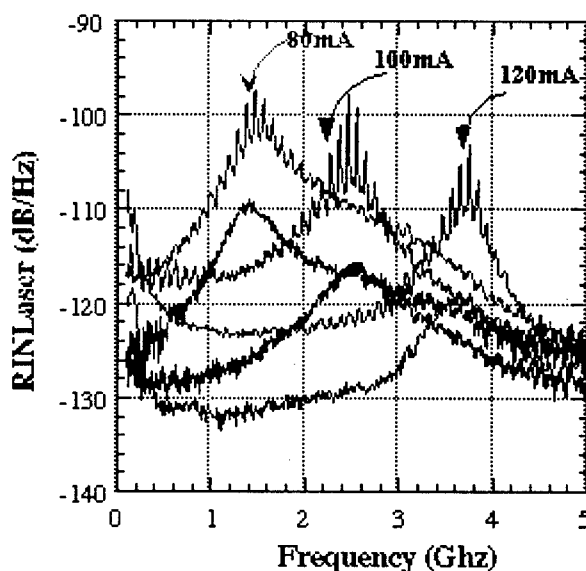


*Figure 14:* Effect of isolator on RIN of 600 μm ring laser at different drive currents. Lower curves with isolator.

The intensity noise of both beams of ring lasers has been measured separately vs. drive current for various device sizes and structural angles. A typical RIN result for a 600 μm ring laser is shown in Figure 15. For high drive currents, most ring laser RINs tend to saturate at -130 dB/Hz at 250 MHz. These WDRLs are bidirectional devices, not unidirectional as in II.1.1.
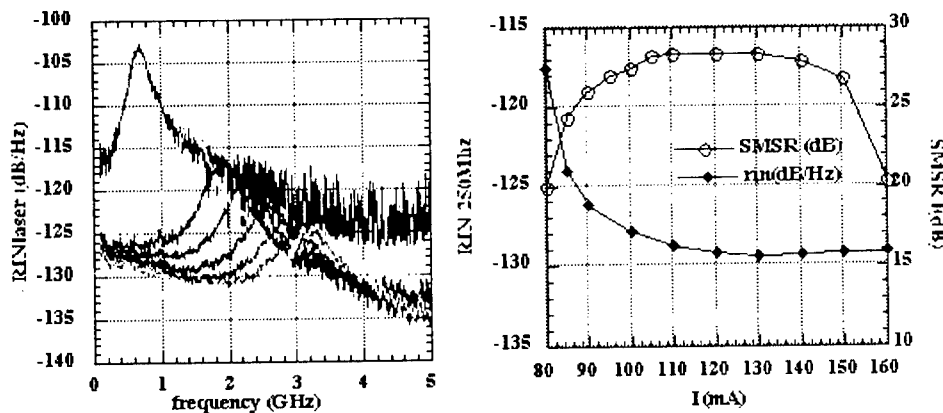


*Figure 15:* (A) 600 μm ring laser RIN vs. I (Ith 80mA), increment 10 mA. (B) SMSR and RIN (250MHz) vs I.

## Temperature Measurements

The triangular ring lasers were placed in a custom designed Liquid Nitrogen dewar, cooled to -100°C, and allowed to warm up to room temperature. The laser was biased at a fixed output power, and the pulsed optical spectra were recorded vs. temperature. SMSR vs. temperature for a 600 μm ring laser is shown in Figure 16, while the pulsed PI vs. temperature graph is shown in Figure 17.
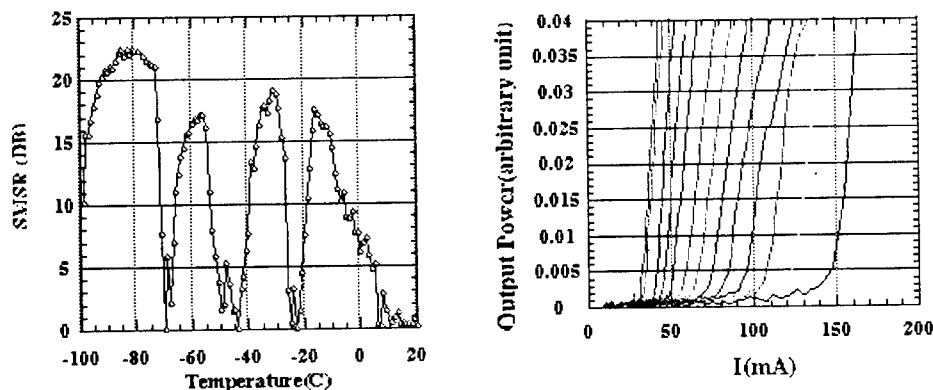


*Figure 16, Left:* SMSR vs. temperature for a 600 μm ring laser.
*Figure 17, Right:* 600 μm ring laser pulsed PI vs temperature -100°C to 20°C, increment 10°C

The characteristic temperature T0 can be calculated from the threshold current values to be 78K. The ring laser maintains fairly good SMSR between mode hops. Compound cavity effect and spectral hole burning have been identified as the factors affecting ring laser spectra, with compound cavity effect playing the dominant role.

12

## II.1.3 Microwave Modulation Properties

A study of the modulation properties of WDRLs was completed by M. Leary [1]. The main objective was to determine whether there were any unique properties of WDRLs which would have a significant effect on the modulation bandwidths of diode lasers in this configuration. To enable direct probing of the devices at GHz bandwidths required changing the process to place both contacts on the top surface where they would be accessible to microwave coplanar probes. Figure 18 shows the resultant geometry of WDRLs suitable for coplanar probing as developed by Leary. The details of the considerable process development necessary to achieve the results in Figure 18 are contained in Reference [1].



(a)          (b)

(c)          (d)
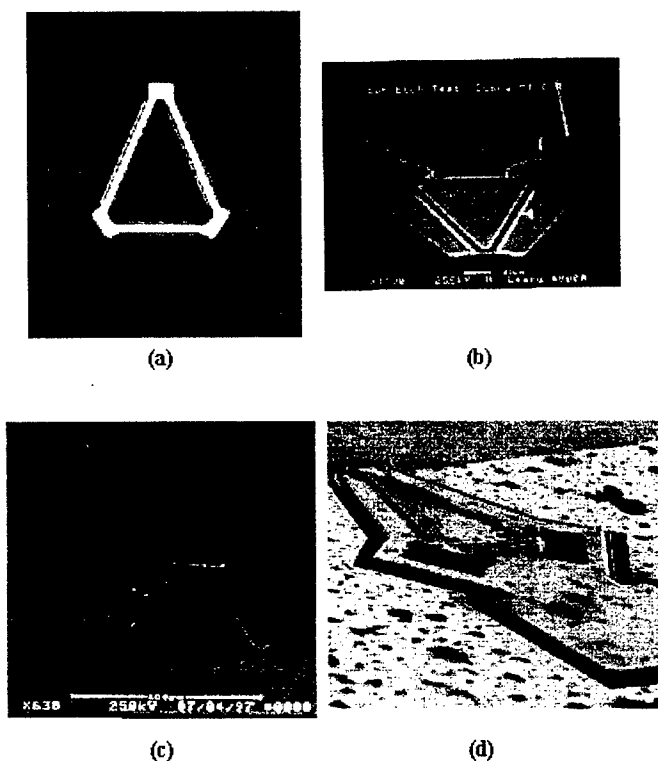
*Figure 18:* *Microscope images depicting various stages in the fabrication process. (a) after lithography to define master mask (b) after ridge etch (c) after contact window etch (d) completed device.*

Both relative intensity noise (RIN) and direct modulation measurements were made on a variety of WDRLs and Fabry Perot lasers on the same chip On these chips, the mirrors were rougher than our normal process, hence threshold currents were higher than normal. However, good comparisons could be made between WDRL devices of various structure angles and Fabry Perot devices. The major result is that WDRLs exhibited comparable modulations bandwidths to the Fabry Perot devices. WDRL modulation bandwidths of 9 GHz were measured. This is a very good value for devices this large (600 μm long). It should be noted that all WDRLs in Leary's study were bi-directional and relatively long. The direct modulation response of an 8° 600 μm WDRL is shown in Fig 9 of Appendix 2 and the results from a series of devices are shown in Fig 10 of Appendix 2. A more detailed description is given in Appendix 2.

## II.1.4 Modeling of Unidirectional Operation

J. M. Lee completed the first three-dimensional finite-element modeling of the fields in abrupt dielectric waveguide structures used to achieve unidirectional operation in WDRLs. Her results are described in Appendix 1. Figures 8 - 11 (Appendix 1) constitute a first-principles computational verification of the asymmetric reflectivity at an abrupt step in a dielectric waveguide. Figure 8 (Appendix 1) shows the standing wave caused by reflections at a step discontinuity. The reflection coefficient can be computed from the standing wave pattern. Figure 9 (Appendix 1) shows the asymmetric nature of the reflection coefficients for waves incident from the narrow and wide sides of the step. Figure 10 (Appendix 1) shows an alternative method for determining reflection coefficient for a step waveguide transition using the relative amplitude of an incident pulse of light and its reflected component. Figure 11 (Appendix 1) shows that after accounting for radiation loss, the reflectivity for a wave incident from a wide to a narrow guide is about twice as large as for a wave incident from a narrow to a wide waveguide. The reflectivity difference of .1% is sufficient to create a large difference in powers for waves circulating in opposite senses in the ring cavity.

## II.2 Packaging Development

Karen Wilson completed an extensive study of WDRL arrays and flip-chip mounting for passive alignment of arrays to optical fibers. The results are contained in her Ph.D. Thesis [2].
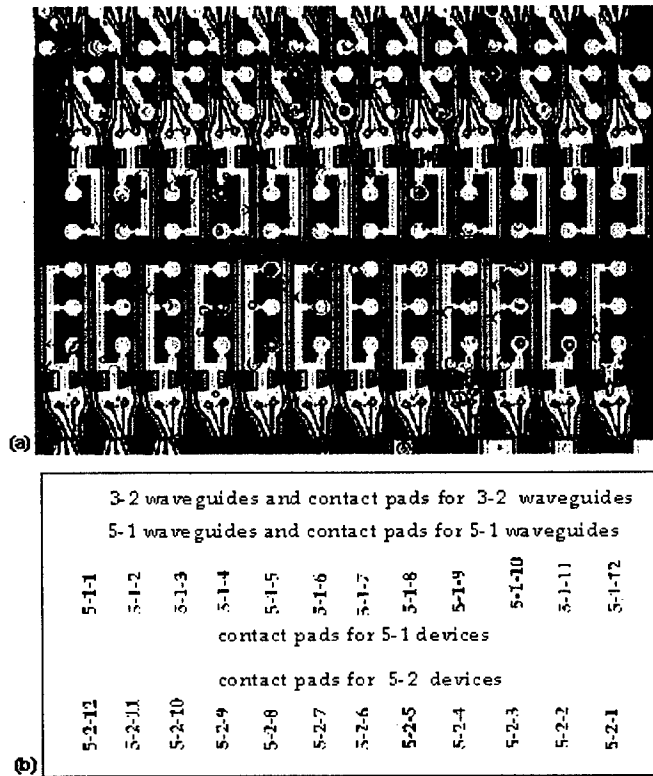


**Figure 19.** (a) Optical micrograph and (b) schematic layout of lapped. Generation 2 10° Waveguide Diode Ring Lasers (WDRL) Array (3-4(A): 5-1 and 5-2).
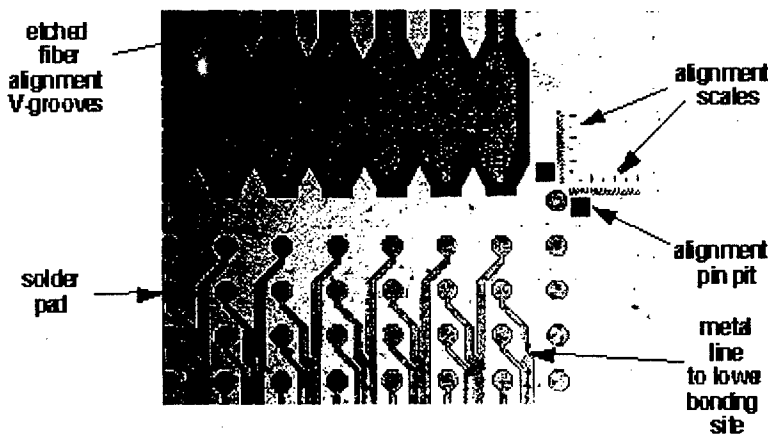


**Figure 20.** Substrate bonding site.

The arrays consisted of twelve WDRL devices, some coupled to output waveguides. Figure 19 shows a top view of a chip containing two arrays of WDRLs, one array with output waveguides, and one without. There are 84 pads for solder balls which are deposited on a mating Si motherboard using a solder-jetting technique. A partial view of the Si motherboard is shown in Figure 20.

Aside from pads for solder balls and metal contact traces, the motherboard contains etched V grooves to align the fibers from the ribbon cable, measurement scales, and a wide wicking groove (running horizontally across the V grooves) to collect excess fiber bonding epoxy.
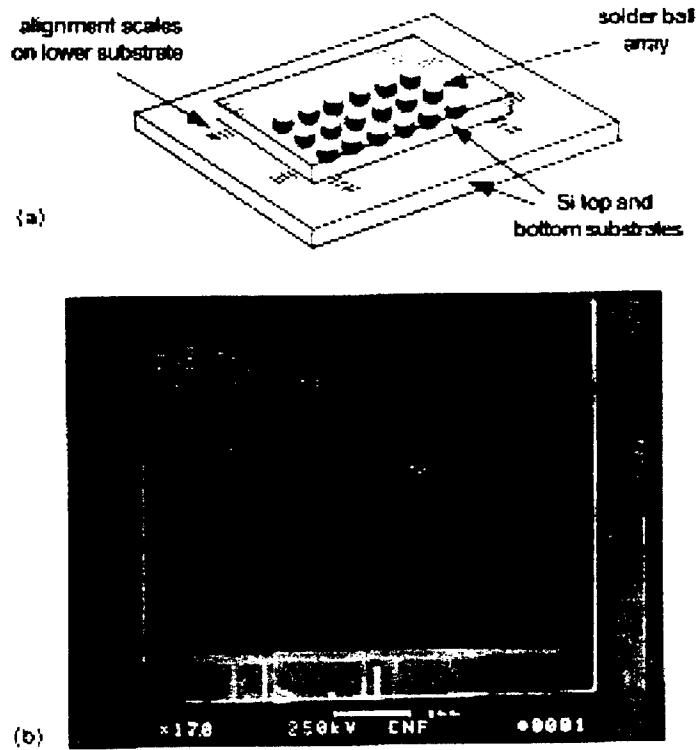


*Figure 21.* *(a) Schematic diagram and (b) SEM picture of Si-to-Si flip-chip mounted test substrate with alignment scales near corners.*
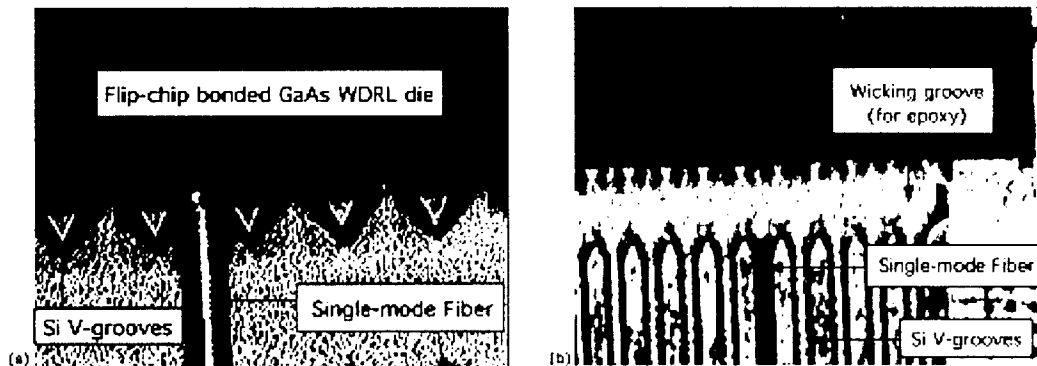


*Figure 22.* *(a) 50X and (b) 20X magnification optical microscope pictures of single-mode fiber placed in Si motherboard V-groove to show butt-coupling and alignment to the GaAs Waveguide Diode Ring LED.*

Figure 21 shows a schematic diagram of the bonding arrangement and Figure 22 shows a mounted GaAs die with one single mode fiber in place.

This work tested the state-of-the-art in solder ball jetting techniques, as each motherboard chip needed 2349 solder balls, and there were 16 chips per wafer. The solder jetting was done at AMP Inc., and required a day per wafer. The large number of solder balls was caused by the complexity of the various test patterns on the wafer and is not inherent in the technique. In production, most of the test structures would be eliminated, and a single chip could be populated in a few seconds. A chip-to-fiber alignment accuracy on the order of 0.5 μm should be achievable by this approach when all jetting and bonding steps are performed accurately.

## II.3  WDRL-to-Fiber Coupling

Several group members contributed to the understanding of WDRL-to-fiber coupling efficiency. In work prior to this grant, Lau et al [3] computed the three-dimensional patterns of WDRL modes using plane-wave expansion methods. His work was extended to direct computations of near-fields and fiber coupling by H.-R. Jiang. Figure 23 shows Jiang's computed peak butt-coupling efficiency vs. displacement of fiber from laser facet, for a WDRL with 5° structure angle, into a single-mode fiber with 8 μm core diameter. For direct contact, an efficiency of 9.5% is predicted.



**Figure 23.** *0-15 μm butt coupling data, and extrapolation, of a single-mode fiber to a Waveguide Diode Ring Laser.*

**Theoretical Calculation of Coupling Efficiency of Waveguide Diode Ring Laser vs. Orientation of the Observes Field**
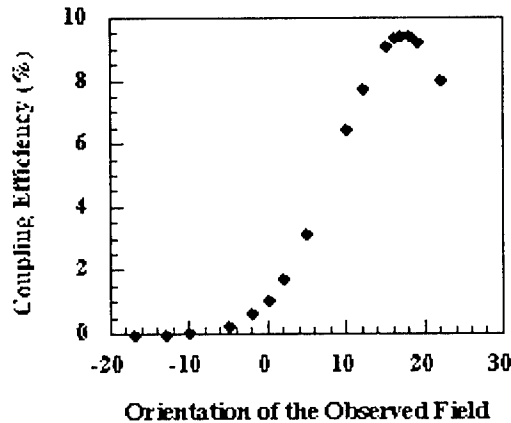


*Figure 24. Angular misalignment of the single-mode fiber cleaved end to the Waveguide Diode Ring Laser facet.*

Figure 24 shows how this efficiency changes with angular misalignment between fiber and laser. Maximum coupling occurs at 17 degrees because that is the angle of the WDRL output beam. Angular misalignment of about ± 5 degrees from 17° results in .5 db increase in coupling loss. Hong Rui's calculations show that the fiber coupling efficiency of low-angle WDRLs is comparable to that of Fabry-Perot lasers.

J. M. Lee did a three-dimensional finite element numerical simulation of the near-field from our ridge waveguide which would be applicable to a Fabry-Perot or waveguide-coupled WDRL. Her computation is more accurate than Hong Rui's, because it takes account of the actual field distribution and not an elliptical gaussian approximation. Lee computed coupling efficiency of about 50% for a butt-coupled single-mode fiber spaced 3 microns from the output source. (See Appendix 1)

M. Leary experimentally measured coupling efficiency to an 8-micron-core fiber for WDRLs with 8° - 17° structure angles. He found 25-30% efficiency after correctable losses in an isolator and absorbing first lens were subtracted. K. Wilson also measured butt-coupling efficiencies of LEDs and WDRLs, but at such large laser-fiber spacings (35 μm and greater) that the low efficiencies of .3 - 3% are not meaningful here.

In summary, butt-coupled single-mode fiber WDRL coupling efficiencies in the vicinity of 20% to 50% should be achievable with careful passive alignment.


## II.4 Materials and Monolithic Integration Studies

We proposed two foci for our materials work. The primary focus was to be growing material for 1.3 μm WDRL fabrication for the rest of the program. This objective was achieved, and 1.3 μm laser material with threshold current density of 1.5 KA/cm², comparable to material we received from Ortel, was grown.

*18*

An exciting packaging and performance possibility arises if we can make WDRLs monolithic on Si substrates, as the substrates can serve as optical benches for fiber attachment - eliminating flip-chip solder-bump or other hybrid packaging technology with a subsequent great reduction in cost and improvement of alignment accuracy and coupling efficiency. In this case coupling efficiency or alignment accuracy will only be determined by fiber eccentricity, as lithography and process tolerances are sufficiently fine to eliminate other sources of misalignment and associated loss. This is in contrast to the hybrid technology described in section II.2, where many other tolerances like solder-ball volume, number of pads, etc. impact coupling efficiency. Under SRC support we have been developing a new monolithic III/V - Si materials structure for this purpose. We proposed that our new strategy can be advantageously combined with ternary nitride compounds GaAsN, GaPN to yield an even better device materials system which is lattice-matched to Si, and possesses a large range of direct-bandgap tunability.

We investigated the ternary nitride system during the first year of the program, and while we made useful research contributions to the understanding of this materials system, concluded that more advanced growth techniques would be necessary than our MOCVD and MBE systems could provide. We therefore used the materials resources in this program to further the GaInP/GaP/Si system being developed for SRC.

Our approach is to develop a pseudomorphic direct bandgap material which can be grown with Si lattice constant and serve as a laser gain medium. Previously, it was shown that smooth GaP could be deposited on 4° off axis silicon using selective area epitaxy MOCVD [2]. Since GaP, like silicon, is an indirect bandgap material, the growth of direct bandgap, strained GaInP quantum wells (QWs) on GaP substrates was investigated. We were successful in 1996 in developing the first direct bandgap material with Si lattice constant. It is an ordered $Ga_{1-x}In_xP$ pseudomorphic quantum well grown on GaP [4]. The GaInP showed strong photoluminescence (PL), however, the change in PL intensity as a function of sample temperature was not like that of a typical QW. Therefore, a model was developed to explain this behavior. The model was based on the theory that the GaInP consisted of distinct regions of ordered (Ga and In in alternate unit cells) and disordered (Ga and In randomly distributed among unit cells) material. Atomic force microscopy (AFM) and scanning electron microscopy (SEM) of the samples indicated that growth proceeded in the Stranski-Krastanov (S-K) mode, meaning that the material first grew in the layer-by-layer growth mode (2D growth) until the strain in the film became so large that islands began to form (3D growth). It was further determined that the islands consisted of ordered material, while the 2D wetting layer was random alloy [6].

Further research focused on investigating the performance of the GaInP materials system in optical device structures. GaP/GaInP was used successfully in an LED structure (Appendix 3). Initial optical pumping experiments on an AlGaP/GaP/GaInP laser waveguide structure were also performed.

# Results in 1998

As mentioned previously, GaP was growth smoothly on silicon substrates by selective area epitaxy. It was not known, however, whether GaInP islands could be grown on a patterned surface. Therefore, GaInP was deposited on patterned GaP substrates. The wafers were patterned with a silicon nitride mask that consisted of alternating "stripes" of exposed wafer and mask material. The mask contained stripes of different size, the width of which varied from 3 μm to 200 μm. Figure 25 shows the effect of stripe width on the formation of GaInP islands.
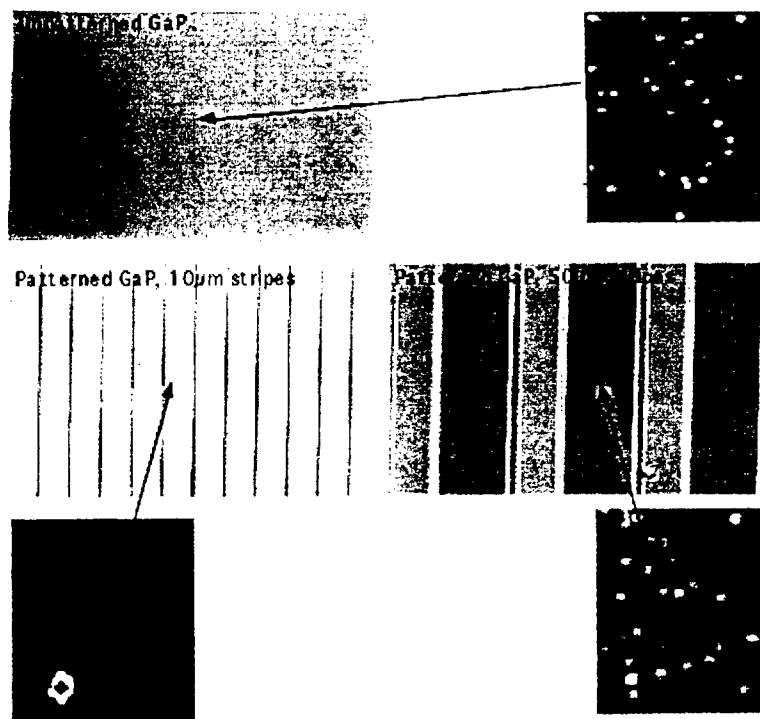


**Figure 25:** *Effect of mask pattern on growth of GaInP islands.*

These samples were grown with a 20 Å cap layer over the GaInP islands so that AFM could be used to study the surface morphology. The photos of the mask pattern are taken using Nomarski phase contrast microscopy. Larger stripe sizes, such as the 50 μm lines shown in the figure, produced an island density that was similar to or greater than that seen on the unpatterned GaP substrate. However, as the line size decreased, the island density also decreased. On the area of the wafer patterned with 10 μm lines, there are very few or no islands on the GaP surface, probably indicating that the growth rate in these areas is greatly enhanced and prevents island formation. PL emission was not observed in regions that did not contain islands. Although the mask pattern could be used to control the density of the GaInP islands, it did not appear to alter the size or shape of the islands.

For the GaP/Si system, the best quality layers were grown in 3 μm wide stripes next to a large, 5 mm wide masked region. Therefore, careful control of the growth parameters will be needed when incorporating the GaP/GaInP system on silicon. Since the growth rate appears to be the controlling factor, altering this parameter should allow growth of islands on smooth GaP deposited on silicon.

Further progress was recently made on improving the optical properties of the GaP/GaInP system.

Previously, good photoluminescence was observed from GaInP islands, however, these results were not reproducible. By altering the growth protocol of the system, films with a 10X improvement in PL intensity were produced, and this result was highly repeatable (see Figure 26).
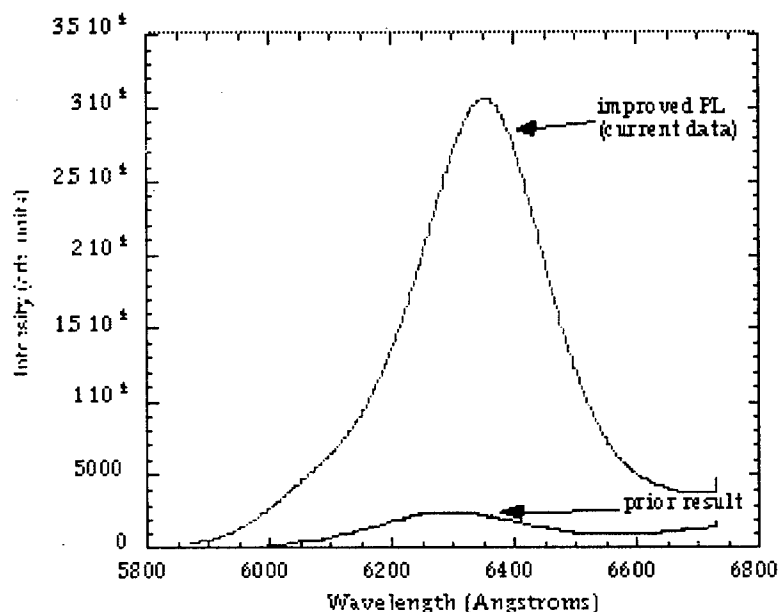


*Figure 26:* Reproducible 10X improvement in luminescence of S-K GaInP/GaP.

The GaInP active region was incorporated into a half-waveguide laser structure. An AlGaP alloy (30%) was chosen as the low index cladding and GaP was chosen as the barrier layer. The half-waveguide structure was tested by optically pumping the sample with a UV laser. The pump light was focused in a stripe on the surface of the waveguide with a cylindrical lens; light emitted from the waveguide was collected at the cleaved edge, or facet, of the sample and sent to a spectrometer. Previously, the structure was pumped using a CW Ar laser at 363 nm. However, the beam from the Ar laser was not powerful enough to generate population inversion in the sample. This is expected, as a typical quantum well laser undergoes inversion at $\sim 10^3$-$10^4$ W/cm$^2$, while the Ar laser has a maximum power density of only $\sim$30 W/cm$^2$. Another problem associated with the earlier optical pumping experiments was that the laser structure was not optimized.

Recent experiments focused on growing an optimized laser structure and testing the optical properties of this improved structure. The thickness of each of the layers in the optimized structure was determined by calculating the spatial overlap of the optical mode and the gain profile. The maximum in the optical field was determined and the GaInP active region was placed at this maximum. Once the optimized structure was grown, it was tested by optical pumping in the same manner as described above. However, a high power, pulsed nitrogen laser (337 nm) was used as the pump source. The maximum power density of this laser is $\sim$3 MW/cm$^2$, which should be sufficient to achieve population inversion in the sample. Initial testing indicated that as the pump power was increased, the emitted light from the sample increased in intensity, but then reached saturation. So, although the sample showed strong PL at 77K, laser behavior was not observed. During this set of experiments, the cleaved facets of the sample served as the mirrors of the laser cavity. Since this may have been a large source of loss, the facets were coated with aluminum. The aluminum mirrors had an 80%

reflectivity compared to the 30% reflectivity of cleaved facets, improving the total cavity reflectivity ~5X. When this structure was optically pumped, two peaks evolved as the pump intensity was increased (Figure 27).
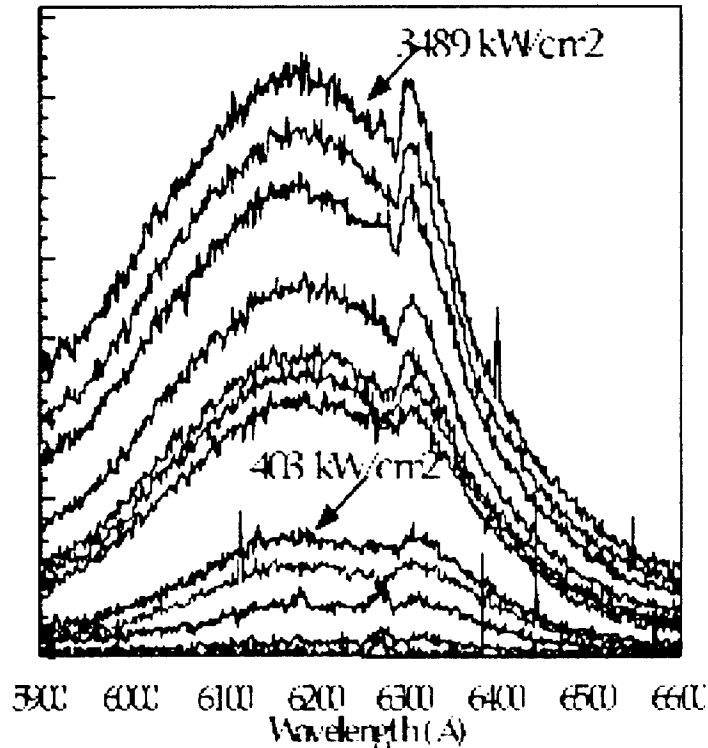


*Figure 27:* High intensity optical pumping of GaP/AlGaP/GaInP laser structure with aluminized mirrors.

A broad peak occurred at 620 nm, while a narrower peak formed at 630 nm. Additionally, the emitted intensity as a function of pump power did not show the saturation behavior that was observed in earlier experiments. This data seems to indicate that stimulated emission is occurring in the material, and, although laser behavior was not observed, that it may be possible to make a laser from this material. The experimental setup of this pumping experiment is currently being altered to optimize the light collected from the sample and to optimize the pump beam geometry. With these improvements, laser behavior may be observed in this material.

# III. Summary and Outlook

This program developed waveguide diode ring lasers (WDRLs) for incorporation into laser modules for applications in data transmission requiring low noise, single mode sources which can be incorporated as arrays into small, inexpensive modules with moderate output powers. Capabilities of WDRLs developed in this program include wavelengths at 1.3 micron and shorter, 30 db side-mode-suppression ratios, tens of milliwatts of output power, relative intensity noise of -150 dbm, threshold current down to 5 mA, direct modulation bandwidth of 9 GHz, electrically-switched beam steering, highly integrable and low-cost manufacturability based on etch-defined optical cavities and planar processing technologies which do not require regrowth, and monolithic integration of lasers, detectors and amplifiers. The key concepts enabling this performance are protected under two patents. Techniques for passive alignment of 12-laser arrays to single mode fiber ribbon were developed. Materials for monolithic lasers on Si were developed which showed stimulated emission and should enable cheap, passive alignment of large laser arrays with single mode fibers.

This program suffered a major setback when funding for the third year was deleted towards the close of the second year due to the Air Force decision to terminate photonics work. This necessitated a major reduction in the scope of the work, led to the dismissal of 6 people in the group and prevented the full achievement of many of the goals of the program. Nevertheless many major milestones were achieved, including fabrication of the first well-behaved 1.3 micron wavelength WDRLs, showing that good, all-etched laser cavities for the GaInAsP/InP system are possible. We also did the first experimental measurements of the modulation and noise properties of waveguide diode ring lasers. These measurements gave the important results that unidirectional WDRLs do indeed show very low noise, as originally conjectured. The RIN decreases by 20 db for unidirectional over bidirectional operation, with -150 dbm RIN demonstrated for a single mode laser. While low RIN has been seen in Fabry-Perot lasers, these are multimode devices which show much more noise when a single mode is isolated. The modulation measurements showed that WDRLs have similar modulation bandwidths to Fabry-Perot devices, with 9 GHz -3 db bandwidth demonstrated for 600 micron long WDRLs. Since WDRLs can be made much smaller, they will show the same ~30 - 40 GHz bandwidth limitations as do high speed Fabry-Perot devices.

Process improvements continued to reduce threshold current, with 5 mA now demonstrated. But we know that further process improvements can be made to enable smaller Ith. Present devices have current leakage paths which are significant and can be eliminated by mask redesign. Hence thresholds in the 2 mA range are probably practical.

We discovered a new phenomenon: unidirectional beam switching controlled by injection current level. Large beam ratios (45:1) and large switching hysteresis is observed which has obvious and exciting applications in beam routing, optical logic, noise reduction, etc. This unidirectional switching doubles the single-beam power conversion efficiency.

We made major progress towards a monolithic integration of diode lasers on silicon by developing a new, nearly lattice-matched direct bandgap material for Si: the quantum-island GaInP/GaP/Si system. This material has shown stimulating emission at 630 nm. For module development, it promises very cheap and accurate packaging of diode laser arrays to ribbons of single-mode fiber using passive alignment.

Promising avenues which cry for continued exploration include a number of items which were terminated by the funding cut: combined materials/device development to illustrate the achievable properties of 1.3 μm devices including low threshold, unidirectional operation; noise properties under active direct modulation, and optimization of amplifier/laser combinations. The mechanisms of current controlled directional switching need to be understood, controlled, and optimized. And the array packaging for passive single-mode ribbon alignment needs to be completed. The properties of the GaInP/GaP/Si materials system need to be optimized, achievable gain measured, and injection lasers on Si built in this materials system.

In summary, WDRL development for laser modules has progressed to the point where the devices demonstrate a combination of attractive features for low-noise data transmission which are difficult to duplicate in any other single device. These features include moderate output power (10 - 40 mW), low-noise (RIN of -150 dB), single mode operation (~ 50 MHz linewidth), high speed direct modulation (10 GHz or more), planar low cost manufacturability, and monolithic integratability with other components such as amplifiers and detectors. This combination of capabilities is generally not available in either VCSEL or DBR lasers. Devices were demonstrated which simultaneously showed 40 mW output power, ⁻150 db, RIN, and single-mode oscillation. Additional investments in developing WDRL capability would likely pay handsome dividends for applications.

# References:

[1]     "Lasers and Photodetectors for High Speed Monolithic Optoelectronics"; M. H. Leary, Ph. D. Thesis, Cornell University, January 1998.

[2]     "Monolithic Etched-Faceted Triangular Waveguide Diode Ring Laser Arrays for Hybrid Optical Packages using Passive Alignment"; K. I. Wilson, Ph. D. Thesis, Cornell Univeristy, August 1998.

[3]     S. T. Lau and J. M. Ballantyne, IEEE J. Lightwave Technology, 15, 551 (1997).

[4]     "GaInP/GaP Partially Ordered Layer Type-1 Strained Quantum Wells", J. W. Lee, A. T. Schremer, D. Fekete, J. Ballantyne, Appl. Phys. Lett. 69, 4236 (1996).

[5]     "Selective Growth of GaP on Si by MOCVD", J. S. Lee, J. Salzman, J. M. Ballantyne, D. Emerson, J. R. Shealy, J. Crystal Growth 172, 531 (1997).

[6]     "Growth of Direct Bandgap GaInP Quantum Dots on GaP Substrates", J.W. Lee, A.T. Schremer, D. Fekete, J. R. Shealy, J.M. Ballantyne; J. Electr. Materials 26, 1199 (1997).

# IV.  Publications List

[1]     "Selective Growth of GaP on Si by Metal Organic Vapor Phase Epitaxy"; J.-W. Lee, J. Salzman, J. M. Ballantyne, D. Emerson, L. R. Shealy. Abstracts Materials Research Society 1995 Fall Meeting, Boston, EE 3.5 p 706, Nov. (1995)

[2]     "Lasers and Detectors for Integration with HEMT Technology"; J. M. Ballantyne, Invited Paper, Proceedings ARPA/ETO RF-Lightwave Integrated Circuits Workshop, Crystal City, VA, Feb. 15 (1996)

[3]     "Monolithic Semiconductor Ring Lasers"; J. M. Ballantyne, C. Ji, S. T. Lau, J. J. Liang, M. H. Leary, K. Wilson, A. Schremer, Y. Salzman, D. Fekete, Proceedings Book, 1995 ARPA MTO Program Review, Big Sky, MT, July (1995)

[4]     "Photons from the Si Chip?"; J.M. Ballantyne, Poster at International Workshop on Future of Micro-electronics, Porvoo, Finland, Sept. 1996, invited participant.

[5]     "2-D Analysis of a Dielectric Wave-Guide Mirror"; S. T. Lau and J. M. Ballantyne, IEEE J. Lightwave Technology 15, 551 (1997)

[6]     "Unidirectional Operation of Wave-Guide Diode Ring Lasers"; J. L Liang, S. T. Lau, , M. H. Leary, and J. M. Ballantyne, Appl. Phys. Lett. Vol. 70, 1192 (1997)

[7]     "Triangular Shaped Waveguide Diode Ring Laser Fabricated Using Cl2 RIBE in InP/InGaAsP"; C. Ji, M. H. Leary and J. M. Ballantyne, Electronics Letters 33, 493 (1997)

[8]     "Selective Growth of GaP on Si by MOCVD"; J.-W. Lee, J. Salzman, J. M. Ballantyne, D. Emerson, and J. R. Shealy, J. Crystal Growth Vol. 172, p. 53 (1997)

[9]     "GaInP/GaP Partially Ordered Layer Type-1 Strained Quantum Well"; J.-W. Lee, A. T. Schremer, D. Fekete and J. M. Ballantyne, Appl. Phys. Lett. Vol. 69, pps. 4236-8, Dec. (1996)

[10]    "Diode Ring Lasers for Integration with Microwave Circuits"; J. M. Ballantyne, S. Lau and J. Liang, SPIE Proceedings, Vol. 2844, pps 91-96, Technical Conf. on Photonics & Radio Frequency, 7 Aug. (1996)

[11]    "Design of Minimum Threshold Current Triangular Ring Lasers"; S. T. Lau and J. M. Ballantyne, Proceedings IEEE LEOS '96, Vol. 2, pps 136-7 (1996)

[12]    "Growth and Analysis of a Direct-Gap Light Emitting Structure on GaP"; J. W. Lee, A. Schremer, D. Fekete, and J. M. Ballantyne, Proc. IEEE Leos '96, Vol. 2, pps 130-131 (1996)

[13]  "Direct Bandgap Quantum Wells on GaP", J. W. Lee, A. T. Schremer, D. Fekete, J. R. Shealy and J. M. Ballantyne, Control of Semiconductor Surfaces and Interfaces, ed. S. M. Prokes, et al., p. 90 Materials Research Society Symposia Proceedings, vol 448. Pittsburgh, PA: MRS.

[14]  "Growth of Direct Bandgap GaInP Quantum Dots on GaP Substrates"; J. W. Lee, A. T. Schremer, D. Fekete, J. R. Shealy and J. M. Ballantyne, J. Electronic Materials 26, 1199 (1997)

[15]  "Long-Wavelength Triangular Ring Laser"; C. Ji, M. H. Leary and J. M. Ballantyne, IEEE Photonics Technol. Lett. 9, 1469 (1997)

[16]  "Materials and Devices for Silicon On-Chip Interconnect"; J. M. Ballantyne, in "Advanced Interconnects and Contact Materials and Processes for Future Integrated Circuits, ed. S. P. Murarka, et al, Materials Research Society Symposium Proceedings, vol 514, p 83, (1998)

[17]  "Direct Bandgap Material for Optical Interconnect Monolithic on Si"; J. M. Ballantyne (invited talk and poster), 2nd International Workshop on Future Information Processing Technologies, Hokkaido, Aug. 25, (1997)

[18]  "Visible Electroluminescence (630nm) from Direct Bandgap GaInP Quantum Dots Grown on Transparent GaP Substrates"; J. W. Lee, A. Schremer, J. R. Shealy, and J. M. Ballantyne, Conf. Proceedings IEEE LEOS, p. 529, 13 Nov. 1997, San Francisco.

[19]  "GaInP/GaP Quantum Dots - a Material for OEIC on Silicon Substrates"; (invited paper), J. W. Lee, A. Schremer, and J. M. Ballantyne, Optoelectronic Integrated Circuits II, 24 Jan. 1998, San Jose, Photonics West Technical Program, p. 122.

[20]  "Long Wavelength Triangular Shaped Waveguide Diode Ring Laser with Dry Etched Facets"; C. Ji and J. M. Ballantyne, Proc. Advanced Semiconductor Lasers & Applications, p. 9, Digest of the LEOS Summer Topical Meetings, 11 Aug. (1997)

[21]  "Long Wavelength Triangular Ring Laser for Monolithic Integration"; C. Ji, M. H. Leary, and J. M. Ballantyne, Optoelectronic Integrated Circuits II, 28 Jan (1998), Photonics West Technical Program, p. 122.

[22]  "Triangular Ring Laser in InP/InGaAsP"; C. Ji, M. H. Leary and J. M. Ballantyne, Conf. Proceedings IEEE LEOS, p. 7, 10 Nov. (1997)

[23]  "First Principles Analysis of Asymmetric Reflectivity in an Abruptly-Stepped Dielectric Waveguide"; J. Li, A. T. Schremer and J. M. Ballantyne, Conf. Proc. IEEE LEOS, p. 510, 10 Nov. (1997)

[24]  "Direct-Bandgap Material Heteroepitaxial on Silicon for Optical Interconnect"; J. W. Lee, A. Schremer, V. Williams and J. M. Ballantyne, Proceedings, VLSI Multilevel Interconnection Conference, Santa Clara, CA., June (1998)

[25]  "III-V Compound Semiconductor Characterization"; Y. H. Chen, MS Thesis, Cornell University, (Jan 1998)

[26]  "Lasers and Photodetectors for High Speed Monolithic Optoelectronics"; M. Leary, Ph. D. Thesis, Cornell University, (Jan 1998)

[27]  "Monolithic Etched-Facet Triangular Waveguide Diode Ring Laser Arrays for Hybrid Optical Packages using Passive Alignment"; K. I. Wilson, Ph. D. Thesis, Cornell University, (Aug 1998)

[28]  "Monolithic Integration of III-V Compound Light-Emitting Devices in Silicon-Based Electronics"; J.-W. Lee, Ph. D. Thesis, Cornell University, (May 1997)

[29]  "Control of a Ring Laser Direction"; J. M. Ballantyne, J. Liang, and S. Lau, US Patent (1997)

# V. List of Personnel

**The following personnel contributed to work under this contract.**

Dr. Joseph M. Ballantyne, Professor of Electrical Engineering, Cornell University

Dr. Dan Fekete, Visiting Scientist, Cornell University; Associate Professor of Physics, Technion, Israel

Dr. A. Schremer, Research Associate in Electrical Engineering, Cornell University

* Dr. S. T. Lau, Postdoctoral Associate in Electrical Engineering and Graduate Research Assistant in Electrical Engineering, Cornell University

* M. Leary, Graduate Research Assistant in Electrical Engineering, Cornell University

* Karen Wilson, GTE Fellow and Graduate Research Assistant in Electrical Engineering, Cornell University

* J. Lee, Graduate Research Assistant in Applied Physics, Cornell University

Chen Ji, Kodak Fellow and Graduate Research Assistant in Physics, Cornell University

M. Booth, NSF Fellow and Graduate Research Assistant in Physics, Cornell University

Victoria Williams, NSF Fellow, Cornell University

A. Littman, Graduate Research & Teaching Assistant in Physics, Cornell University

Chris Arnold, Undergraduate, Applied & Engineering Physics, Cornell University

Jacob Shkolnikov, Undergraduate, Electrical Engineering, Cornell University

H. R. Jiang, Graduate Research Assistant in Physics, Cornell University

J. M. Li, Research Engineer in Electrical Engineering, Cornell University

* Y. H. Chen, Graduate Research Assistant in Materials Science & Engineering, Cornell University

# Graduate Degrees:

* S. Lau, M. Leary, and K. Wilson completed the Ph. D. degree in Electrical Engineering; J. Lee, the Ph. D. degree in Applied Physics; and Y. H. Chen, the M. S. degree in Materials Science under this program.

# Finite Element Analysis of Dielectric Waveguide Mode Filtering, Asymmetric Reflectivity At Abrupt-Step, Near Field Distribution and Coupling to Optical Fiber

Jianmei Li, A. T. Schremer, J. M. Ballantyne

Electrical Engineering Department, Cornell University, Ithaca, NY 14853

## Abstract

Fundamental mode filtering in rectangular dielectric waveguide is studied by full 3-D finite element simulation. Simulation of guided mode propagation in abruptly stepped rectangular dielectric waveguides gives the first direct evidence of asymmetric reflectivity in these structures. Reflectivity vs. asymmetry and implications for unidirectional ring lasers are discussed. A study of the ridge waveguide mode, near field and coupling to optical fiber is also presented.

## I. Introduction

By achieving unidirectional operation with asymmetric elements which favor one circulating direction over the other in single mode waveguide, the triangular waveguide diode ring laser (WDRL) shows higher spectral purity, lower noise, and higher external efficiency. Because of its unique cavity structure (shown in Fig. 1), a WDRL also has the potential for low threshold operation. Experiments showed that an "optical diode" or tapered waveguides could enhance the asymmetry in the output beams [1] [2]. Unidirectional operation has been reported for both the square ring lasers [3] and the circular ring lasers [4] by providing preferential cross coupling for one circulating direction over the other. A scattering matrix analysis predicted that the two internal powers, which circulate in opposite direction, become asymmetric if a preferential cross coupling of the two circulating directions is introduced [5] [6]. For better understanding the electro-magnetic wave propagation characteristics in these structures, and how much asymmetric cross coupling could be
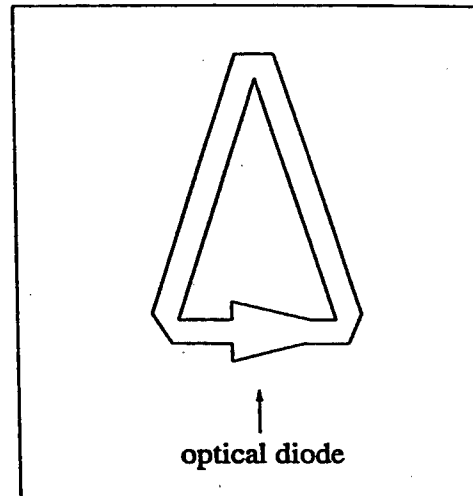
Figure. 1. Schematic of a waveguide diode ring laser with an "optical diode".

introduced by these structures, a 3-D full vector analysis is essential due to the complex geometry with sharp corners.

Accurate numerical analysis methods to understand waveguide propagation characteristics have become more important as computer capabilities have grown and as new developments in integrated optics involve ever more complex structures. Many numerical analysis methods have been developed including the mode expansion propagation method (MEPM) [7], the eigenmode propagation methods (EP) [8], the mode-matching method [9], the "classical" beam propagation method based on Fast Fourier Transformation [10], the Method of Lines BPM [11], the finite difference BPM with scalar analysis [12], semi-vector analysis [13], full-vector analysis [14], and the finite element analysis (FEM) [15]. Among all these
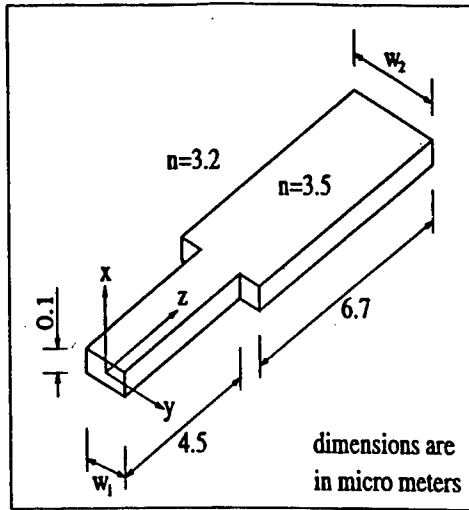
Figure. 2. Waveguide with a step increase in lateral width, comprising the base of the "optical diode".



Figure. 3. Schematic of calculation setup.

| Nodes/wave | Accuracy | Nodes required |
|------------|----------|----------------|
| 10 | 2-8% | 1.5 M |
| 20 | 0.5-4% | 12 M |
| 30 | 0.3-1.5% | 40 M |
| 50 | 0.1-0.6% | 187 M |

Table I. EMLFEX accuracy and memory table for 1500 cubic wavelengths.

methods, discrete modeling codes using finite differences and finite elements are the most general, simple and robust algorithms, and with the help of modern workstations that put near-supercomputer capabilities on the desktop, they can give accurate full-vector waveguide propagation characteristics. Finite differences is the oldest and the most efficient for structurally simple models, while finite elements is better suited to structurally complex models. We chose a commercial time-domain finite element code (EMFLEX) [15] for our WDRL related simulations. In this code, when the time step $\Delta t$ is less than $\Delta x/c$, the fundamental hyperbolicity of Maxwell's equations decouples points separated by $\Delta x$. The discre e problem is then solved locally at each time step. This yields a simple, fast algorithm which eliminates the large system of frequency-domain equations due to the coupling of the fields at all points in space.

## II. Computation Setup

A schematic of a waveguide diode ring laser with an "optical diode" is shown in Fig. 1, which represents the ridge waveguides coupled by etched facets which form the resonant structure. Because the computation time is very
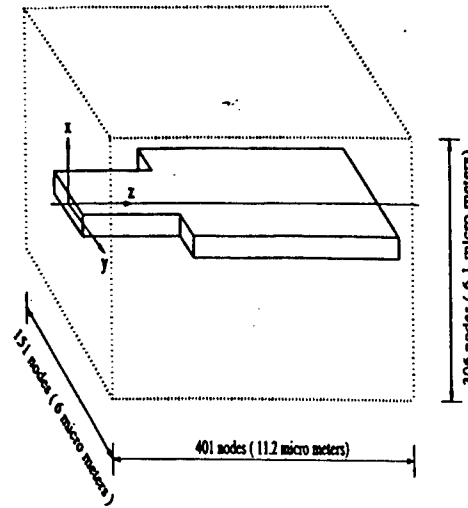
long for a ridge waveguide geometry, a much simpler buried heterostructure (BH) waveguide geometry which preserves the physics but greatly reduces the computation time is used as proof of principle in the asymmetric reflectivity study. We focused on analyzing the abrupt change in lateral waveguide dimension, shown schematically in Fig. 2. The calculation boundary should be big enough to include the waveguide structure and the electro-magnetic field. After trials, we set the calculation size for the case shown in Fig. 2 to $6.1\mu m$ in the $X$ dimension, $6.0\mu m$ in the $Y$ dimension and $11.2\mu m$ in the $Z$ dimension. According to [16], the general accuracy using EMFLEX to model waveguide problems is shown in Table. I. The accuracy is measured by comparison with known analytic solutions and using power conservation (which is usually a lower case estimate of error). The accuracy can vary considerably, even
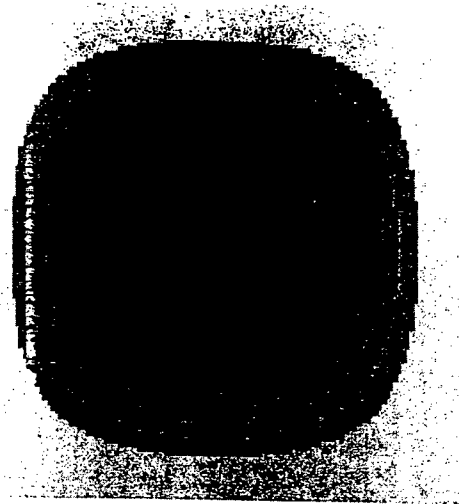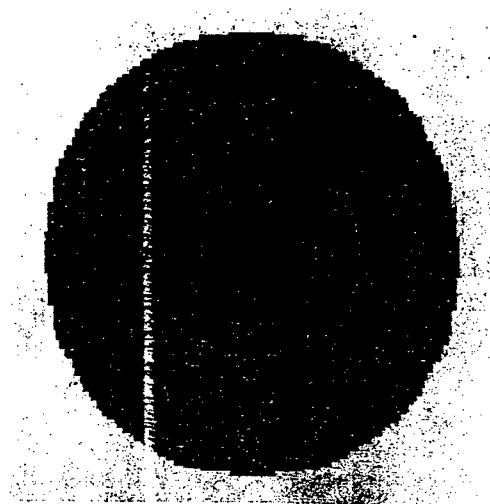
Figure. 4. Initial BH waveguide mode.



Figure. 5. BH waveguide mode after 10.5 $\mu m$ propagation.

with the same node density, depending on the structure of the problem. In order to see the very small reflected wave from the perturbation, high accuracy is necessary for our case, which requires very dense mesh points. Considering the accuracy, memory requirement, and computation time, we choose 306 nodes in the $X$ dimension, 151 nodes in the $Y$ dimension and 401 nodes in the $Z$ dimension. The density of nodes is nonuniform, and is greatest when spatial change is rapid. The computation set up is shown in Fig. 3, it uses $2 \times 10^7$ mesh points and 1GB memory for 32 bit floating point precision with calculating error less than 0.1%. The computation time for $11.0\mu m$ propagation of this setting is about 12 CPU hours on a SUN ULTRA2 workstation with 200MHZ CPU and 2GB RAM, and 30% less on the Cornell SP2 supercomputer single wide node.

## III. Fundamental Mode Filtering

Before studying the reflectivity of the waveguide, we have to calculate the fundamental mode in the waveguide. TE mode calculation is used here. To get the stable fundamental mode in one waveguide structure, the initial mode, which was a 2-D half cosine function in this case, needs to be propagated more than $90\mu m$ down the straight wave guide. The computation was considered complete when no change
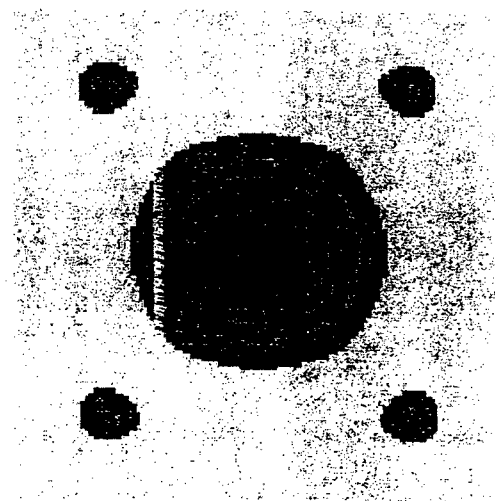


Figure. 6. BH waveguide mode after 21.0 $\mu m$ propagation.

in mode shape was observed over the last $25\mu m$ of propagation, and the plot of the amplitude of the $Y$ component field in waveguide center vs propagation distance is nearly a straight line with variation less than 5%. For a BH waveguide with lateral width $1.0\mu m$ and transverse width $0.1\mu m$, the initial waveguide mode and the waveguide modes after $10.5\mu m$, $21.0\mu m$, and $91.0\mu m$ propagation in the waveguide are shown in Figs. 4 - 7. From the figure, it can be

Figure. 7. BH waveguide mode after 91.0 $\mu m$ propagation.



Figure. 8. Lateral electrical field amplitude along waveguide with $w_1 = 1\mu m$ and $w_2 = 2\mu m$.
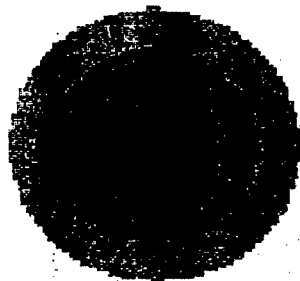
seen that the higher order mode energy is filtered out. This computation takes nearly 120 CPU hours on our SUN ULTRA2 workstation, and was accomplished by breaking the problem into 10 smaller ones, each $10\mu m$ in length. The computation time is proportional to the total number of nodes and the number of time steps, the latter being proportional to the longitudinal length. Thus the computation time is proportional to the square of the longitudinal length when the lateral and transverse structures are fixed, and this was verified by our computations. We also found by experimental computations that the mode shapes and Poynting vector integral at different propagation distances match very well by the two methods (breaking or not breaking a long propagation into smaller problems). In order to study the asymmetric reflectivity, two other stable modes with the same transverse widths and lateral widths equal to $2.0\mu m$ and $3.0\mu m$ were also calculated.

By studying the data of this mode filtering calculation, we understand how the mismatched mode propagates and is filtered in real waveguide, and what is the necessary length of the coupling waveguide. We will come back to this point later.
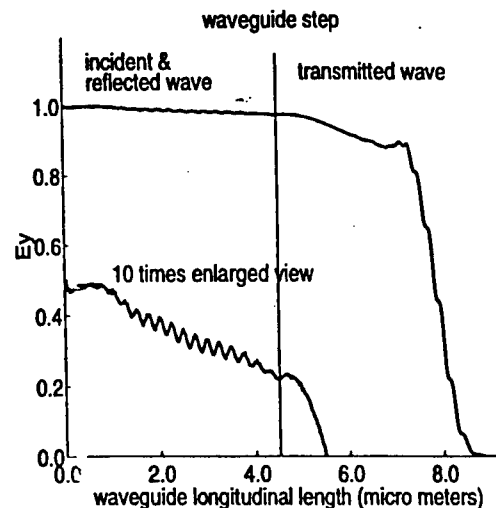
## IV. Asymmetric Reflection At the Abrupt-step

Injecting the stable mode into the waveguide shown in Fig. 2, we compute the incident, reflected and transmitted waves of this waveguide structure. The amplitudes are shown in Fig. 8. $E_y$ is the amplitude of TE mode lateral electrical field in the center of the waveguide averaged over one wave cycle, the wavelength is $1.55\mu m$. The standing wave pattern to the left of the waveguide step represents the interference of the energy coupled into backward propagating modes and the original forward propagating mode. The origin of the backward propagating modes is reflection of the single forward propagating mode at the abrupt step. The computation stopped before the reflected field hit the starting waveguide surface, so the beginning part of the curve is flat, representing the traveling wave amplitude. Note that the noise at $7 - 8\mu m$ is due to the program's end calculation error. The reflection coefficient representing the power reflected at the waveguide step and coupled in to the backward propagating mode can be found from the amplitude of the standing wave pattern; it is 0.0025 for this structure, and 0.0036 for the reverse case (from
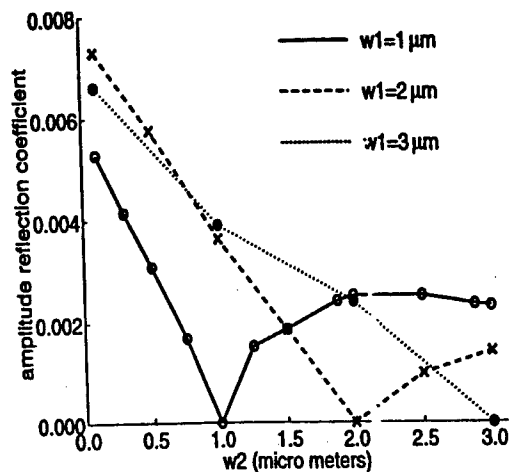
A1-4

Figure. 9. Amplitude reflection coefficient for energy coupled into the backward propagating mode vs geometry of the model waveguide (cf. Fig. 2)



Figure. 10. The reflected and transmitted pulse generated by propagating a single mode pulse through the abrupt step. Above: full view of the pulse; Bottom: enlarged view for the reflected pulse.

$2\mu m$ to $1\mu m$). The reflection from a $1\mu m$ wide waveguide to a $2\mu m$ wide waveguide is about 30% smaller than from a $2\mu m$ to $1\mu m$ wide waveguide. For one amplitude reflection coefficient calculation, the computation time is 10 CPU hours. The amplitude reflection coefficients computed from a series of data similar to Fig. 8 for the standing wave pattern for $w_1 = 1, 2$ and $3$ $\mu m$, with $w_2$ as a variable, are shown in Fig. 9. Note the asymmetry of the curves in Fig. 9 about the zero reflection point ( no width step). This shows the asymmetric reflectivity between propagation into a narrower as opposed to a wider waveguide.

However, in this computation, because the reflected energy does not match the waveguide fundamental mode, some of the reflected energy will be filtered out. The amplitude reflection coefficient calculated by the previous method is only correct close to the waveguide perturbation. In order to study the filtering of the reflected energy, a pulsed stable fundamental mode is injected into the waveguide. By choosing the right propagation time step, the reflected and transmitted pulse are simulated and shown in Fig. 10. From the figure we can see the propagation of the reflected pulse stopped
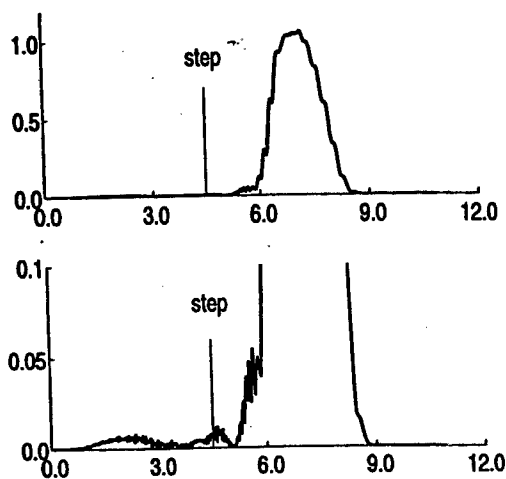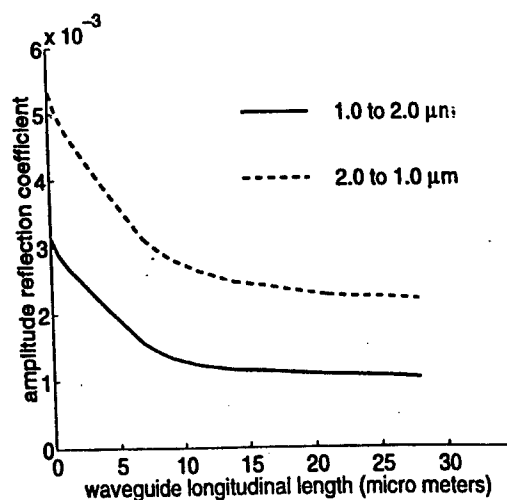


Figure. 11. Amplitude reflection coefficient for energy coupled into the backward propagating guided mode using the Poynting vector integral.

before it hit the starting waveguide surface. Using the field in the middle of the reflected pulse as the initial mode, and propagating this mode down the waveguide as continuous wave, the reflection coefficient calculated by the Poynting vector integrals of the reflected energy at different propagation distance are shown in Fig. 11. The amplitude reflection coefficients for this stable reflected energy are 0.0010 for the reflection from $1.0\mu m$ to $2.0\mu m$ and 0.0022 for the reflection from $2.0\mu m$ to $1.0\mu m$. The asymmetry character is not changed. In fact, the ratio of backward to forward reflectivities grows larger as one moves further from the steps, and for this model waveguide reaches values for stable modes at about 10 - 15 $\mu m$ from the step. The actual values of reflectivity, reflectivity ratio, and decay length will depend on the details of each waveguide structure. Hence computations for actual ridge waveguide diode structures must be done to predict the properties of actual WDRLs. Such computations are within the capacities of parallel supercomputers using the present code.

The above results clearly confirm the asymmetric nature of the "optical diode". According to the scattering matrix analysis [5], 0.1% difference in the forward power coupling coefficients could yield very high internal power ratio for the counter propagating waves. This leads to asymmetric oscillating strengths of the counter propagating beams in the ring laser, with the direction receiving stronger cross coupling becoming the dominant beam. For large asymmetries, the laser can be considered to be unidirectional.

## V. Near Field of Ridge Waveguide

Studying the near field of the laser waveguide facet is important to get efficient coupling between waveguide and optical fiber. A model typical of the Cornell ring laser waveguide structure is shown in Fig. 12, the wavelength is $0.81\mu m$ and the parameters are shown in Table. II. The calculated TE fundamental mode is shown in Fig. 13 (2-D view) and in Fig. 14 (view in two cross directions). In this calculation, we use around 10 nodes per
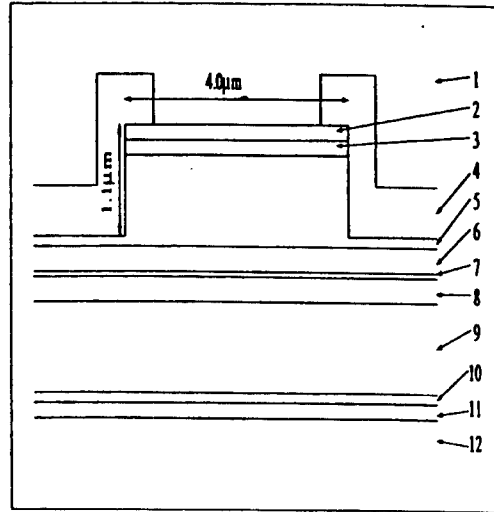


Figure. 12. Layer structure of the Cornell ridge waveguide.

| | Layer | $(\mu m)$ | Index |
|---|---|---|---|
| 1 | Air | | 1.0 |
| 2 | Contact[GaAs] | 0.15 | 3.68 |
| 3 | Graded[AlGaAs(2-70)] | 0.15 | 3.68-3.17 |
| 4 | Oxide[$SiO_2$] | 0.5 | 1.5 |
| 5 | Cladding[AlGaAs(70)] | 0.9 | 3.17 |
| 6 | Index[AlGaAs(70-30)] | 0.25 | 3.17-3.43 |
| 7 | QW[AlGaAs(8.5)] | 0.01 | 3.62 |
| 8 | Index[AlGaAs(30-70)] | 0.25 | 3.43-3.17 |
| 9 | Cladding[AlGaAs(70)] | 0.9 | 3.17 |
| 10 | Graded[AlGaAs(70-2)] | 0.12 | 3.17-3.68 |
| 11 | Buffer[GaAs] | 0.15 | 3.68 |
| 12 | substrate[GaAs] | | 3.68 |

Table II. Parameters of model ridge waveguide laser structure in Fig. 12.

wave length in $X$ dimension, 2.5 nodes per wave length in $Y$ dimension, and 10 nodes per wave length in $Z$ dimension. Even with this very low accuracy set up, the calculation time is about 13 CPU hours for $12\mu m$ propagation. And the calculation time will increase significantly when mesh density is increased. In this case, the initial 2-D half cosine function was propagated 7 sections, each of $12\mu m$ long to get a stable mode.
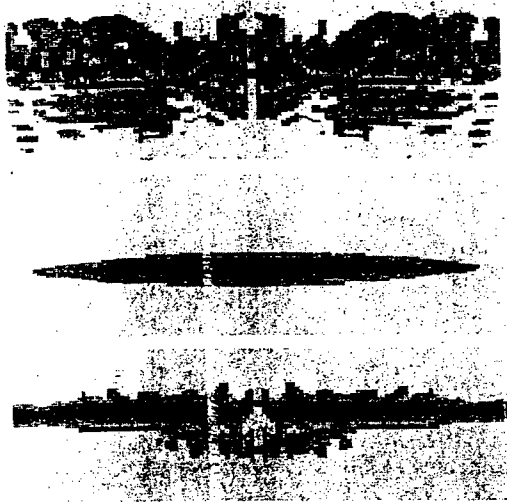
A1-6

Figure. 13.   2-D view of Cornell ridge waveg-
uide TE fundamental mode. Above: $X$ compo-
nent of the electric field amplitude, maximum
amplitude value is 0.0034; Middle: $Y$ compo-
nent of the electric field amplitude, maximum
amplitude value is normalized to 1.0; Bottom:
$Z$ component of the electric field amplitude,
maximum amplitude value is 0.0167.



Figure. 14.   1-D view of Cornell ridge waveg-
uide $Y$ component of TE fundamental mode,
above: in transverse direction, bottom: in lat-
eral direction.
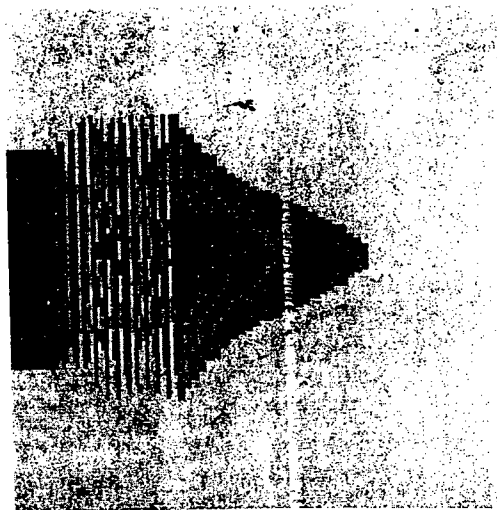


Figure. 15.   Lateral view of the intensity of the
near field of Cornell ridge waveguide.
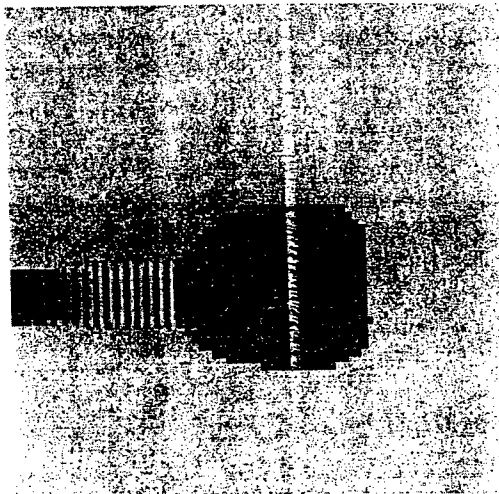


Figure. 16.   transverse view of the intensity of
the near field of Cornell ridge waveguide.

For Fabry-Perot laser cavity, the 3-D near
field is shown in Fig. 15 for lateral cross section
and Fig. 16 for transverse cross section. From
the figure, the field transmitted into the air can
be seen. The standing wave pattern resulting
from the superposition of the forward propagat-
ing fundamental mode and the reflected field
at the waveguide facet is shown also. The 2-D
cross section view of the near field on the out-
put side of facet, $1.0 \mu m$ from facet, $2.0 \mu m$ from

Figure. 17. Y component of the rear field of Cornell ridge waveguide at the output facet.
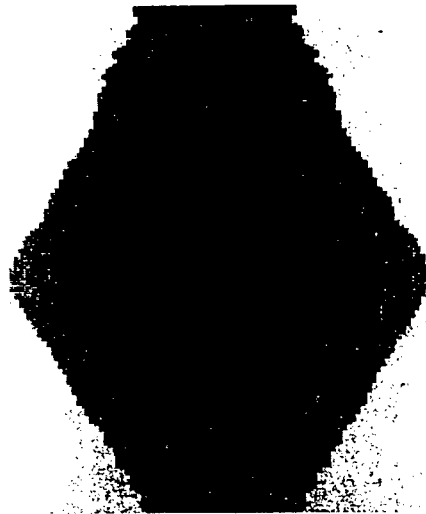


Figure. 19. Y component of the near field of Cornell ridge waveguide 2μm from the facet.



Figure. 18. Y component of the near field of Cornell ridge waveguide 1μm from the facet.
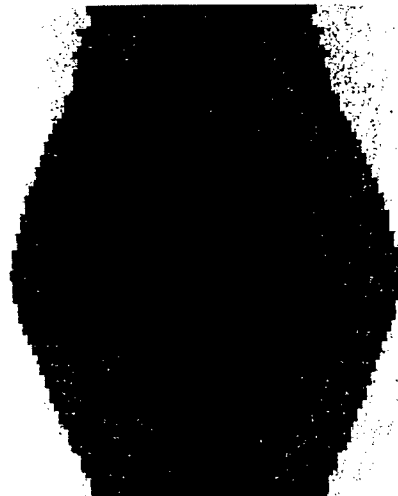


Figure. 20. Y component of the near field of Cornell ridge waveguide 3μm from the facet.

facet, 3.0μm from facet, and 6.0μm from facet are shown in Figs. 17 - 21. In Figs. 19 - 21, note that the calculation boundaries are not totally absorbing, as some reflected "wiggles" in the mode shape are observed near the top and bottom.

For one ring laser corner, the near field is shown in Fig. 22 and Fig. 23.

## VI. Coupling From Ridge Waveguide to Optical Fiber

From the computations of the ridge waveguide near field, it can be seen that the transverse dimension of the mode expands quickly after transmition into the air. The mode shape becomes nearly round at 3μm from the facet, which best matches the round fiber mode shape.

Figure. 21. $Y$ component of the near field of Cornell ridge waveguide $6\mu m$ from the facet.
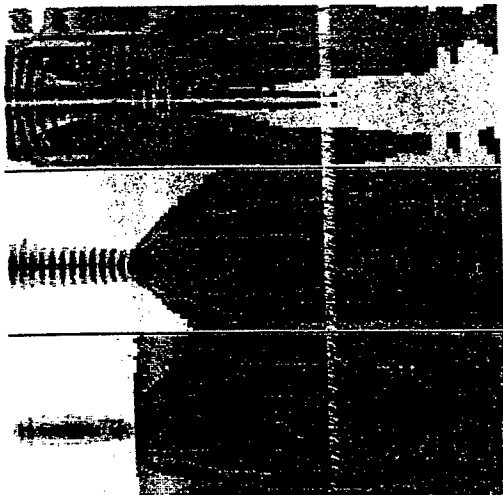


Figure. 22. Lateral view of the near field of Cornell ring laser corner. Above: $X$ component of the electric field amplitude, the maximum amplitude is 0.0032; Middle: $Y$ component of the electric field amplitude, the maximum amplitude is normalized to 1.0; Bottom: $Z$ component of the electric field amplitude, the maximum amplitude is 0.1453.
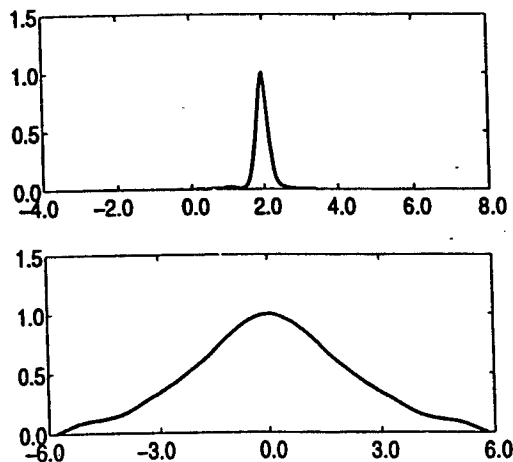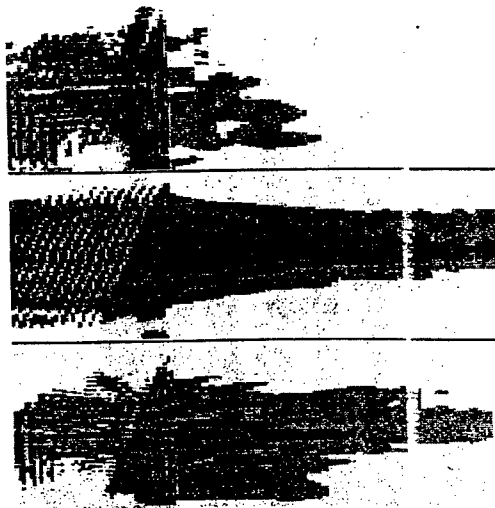


Figure. 23. Transverse view of the near field of Cornell ring laser corner. Above: $X$ component of the electric field amplitude, the maximum amplitude is 0.0023; Middle: $Y$ component of the electric field amplitude, the maximum amplitude is normalized to 1.0; Bottom: $Z$ component of the electric field amplitude, the maximum amplitude is 0.2931.

By performing a calculation which includes the laser waveguide, air gap and optical fiber, we can calculate the coupling coefficient $\kappa$ close to the optical fiber input facet directly using Equation. 1.

$$\kappa = \frac{Poynting\ integral\ energy\ in\ fiber}{Poynting\ integral\ energy\ in\ waveguide}$$
(1)

For a round optical fiber with core diameter equal $8.3\mu m$, core index equal 1.4875, and cladding index equal 1.4823, the coupling coefficient near fiber input facet is 54.87% when the fiber is located $3\mu m$ from the laser waveguide facet. This number will decay along the fiber propagation direction as some of the mismatched energy will radiate. At $7\mu m$ from fiber facet, the coupling coefficient is 51.24%. Because of the mode expansion, the calculation boundary should be increased to get an accurate result when propagating further. Hopefully, with the help of super computer, we can

A1-9

get the stable coupling coefficient in the near future.

## VII. Conclusion and Acknowledgments

We conclude that finite element analysis using a code like EMFLEX is a useful tool for analyzing complicated abrupt transitions in dielectric waveguide for extracting scattering loss, coupling coefficients, mode filtering length and transient and stable mode shapes. We applied this approach to study abrupt asymmetric waveguide transitions and showed that such transitions act as asymmetric reflectors. We can clearly see the small standing waves due to steady state reflection from such step and can directly observe the amplitudes of reflected pulses. The approach also allows one to follow the decay of unstable mode shapes into stable guided modes as energy propagates away from an abrupt waveguide step, and thereby extract decay length of unstable modes and coupling coefficient for stable guided modes. The technique is also suitable for computing laser near fields and coupling coefficients to optical fiber. We expect this will be a useful calibration to check quicker 3-D plane wave expansion techniques for computing coupling between the crescent-shaped output fields of WDRLs and optical fiber.

We successfully broke up large problems into a series of smaller ones to greatly reduce memory requirements and computation time. The results reported here tax the capabilities of today's high-end workstations.

For accurate study of the asymmetric reflectivity of small triangular ring laser cavities, a simulation which includes the whole ring may be necessary, because the edges of the ring may be too short to filter the reflected mode shape, thus invalidating a scattering matrix analysis. Such a computation should also probably include the spatially nonuniform gain of the laser medium. For this huge numerical problem, paralleled code on an array of workstations or multi-node super computer is necessary.

## References

[1] J. Liang, S. Lau, M. Leary, and J. Ballantyne, "Unidirectional operation of waveguide diode ring lasers", Appl. Phys. Lett., 70(10), pp. 1192-1194, 1997.

[2] A. Behfar-Rad, S. S. Wong, and J. M. Ballantyne, Proceedings of the IEDM (IEEE, Piscataway, NJ, 1990), vol. 2, p. 393.

[3] S. Oku, M. Okayasu, and M. Ikeda, IEEE Photonics Technol. PTL-3, pp. 1066 (1991).

[4] J. P. Holimer, G. A. Vawter, and D. C. Craft, Appl. Phys. Lett. 62, pp. 1185 (1993).

[5] S. Lau, T. Shiraishi, and J. Ballantyne, "Scattering Matrix Analysis of a Triangular Ring Laser", J. Lightwave Tech., 12(2), pp. 202-7, 1994.

[6] Stanley T. Lau, Modelling of a Dielectric Waveguide Mirror with Application to Diode Ring Lasers, Ph.D. thesis, Cornell University, Ithaca, New York, 1995.

[7] J. Willems, J. Haes, and R. Baets, "The bidirectional mode expansion method for two dimensional waveguides: The TM case," Opt. Quantum Electron., Special Issue on Optical Waveguide Theory and Numerical Modeling, 27(10), pp.995-1008, 1995.

[8] G. Sztefka and H. Nolting, "Bidirectional eigenmode propagation for large refractive index steps," IEEE Photon. Technol. Lett., vol. 5, pp. 554-557, 1993.

[9] M. Amann, "Rigorous waveguide analysis of the separated multiclad-layer stripe-geometry laser," IEEE J. Quantum Electron., vol. 22, pp. 1992-1998, 1986.

[10] M. Feit and J. Fleck, "Light propagation in graded-index optical fibers," Appl. Opt., vol. 17, pp. 3390-3998, 1978.

[11] J. Gerdes and R. Pregla, "Beam propagation algorithm based on the method of lines," J. Opt. Soc. Amer. B, vol. 8, pp. 389-394, 1991.

[12] T. Rasmussen, J. Povlsen, and A. Bjarklov, "Accurate finite difference beam propagation method for complex integrated optical

structures," IEEE Photon. Technol. Lett., vol. 5, pp. 339-342, 1993.

[13] M. Stern, "Semivectorial polarized finite difference method for optical waveguides with arbitrary index profiles," IEE Proc., 135(1), pp. 56-63, 1988.

[14] G. Hadley, R. Smith, "Full-Vector Waveguide Modeling Using an Iterative Finite-Difference Method with Transparent Boundary Conditions," J. of Lightwave Technology, 13(3), 1995.

[15] G. Wojcik, J. Mould Jr. and L. West, "Time-Domain Finite Element Modeling of 3D Integrated Optical Devices," Integrated Photonics Research Tech. Digest, W.D.1. Optical Society of America, eds., pp. 112-115, 1993.

[16] Private conversation with L. West in Integrated Photonic Systems Inc. who provide the consulting service for Cornell.

# Modulation Properties of Triangular Waveguide Diode Ring Lasers

Michael H. Leary, Chen Ji, Michael F. Booth, and Joseph M. Ballantyne
Cornell University, Department of Electrical Engineering
Ithaca, NY 14833

## 1. Introduction

By combining diverse electronic, optical, and optoelectronic functions on a single, manufacturable chip, optoelectronic integrated circuits (OEICs) promise to bring the high performance potential of optical interconnect down to an affordable price point. Such systems will require high performance, monolithically integrable components, particularly lasers and photodetectors. One particularly promising laser source for these applications is the triangular cavity waveguide diode ring laser.[1],[2] These novel lasers have high side mode suppression ratios and the potential for low noise operation [3] and are fabricated with self-aligned, dry etched facets [4] which make the structure highly manufacturable. In addition, this structure features a geometrically adjustable cavity Q that does not require facet coatings to achieve unusually high or low cavity reflectivities [4],[1] and a planar cavity for ease of passive fiber coupling.

The work to date on the ring lasers has focused on DC or low frequency characteristics. For the devices to be useful in high speed data transmission applications, the high frequency modulation characteristics must be studied. We present here what we believe to be the first report of the direct modulation bandwidth of etched-facet semiconductor waveguide diode ring lasers. In this work, we studied the modulation properties of the lasers through both relative intensity noise (RIN) measurements and direct modulation response measurements. The RIN measurements were used to determine the effective differential gain and modulation K-factor, which were then used to predict the direct modulation response. The direct modulation measurements were performed to confirm the predictions from the RIN measurements and to estimate the parasitic capacitance and resistance of the laser structure. The measurements were performed both on ring lasers and on etched facet Fabry Perot lasers fabricated alongside the rings on the same chip. The analysis is focused on searching for any differences between the ring and Fabry Perot lasers that might arise from the unique ring cavity structure.
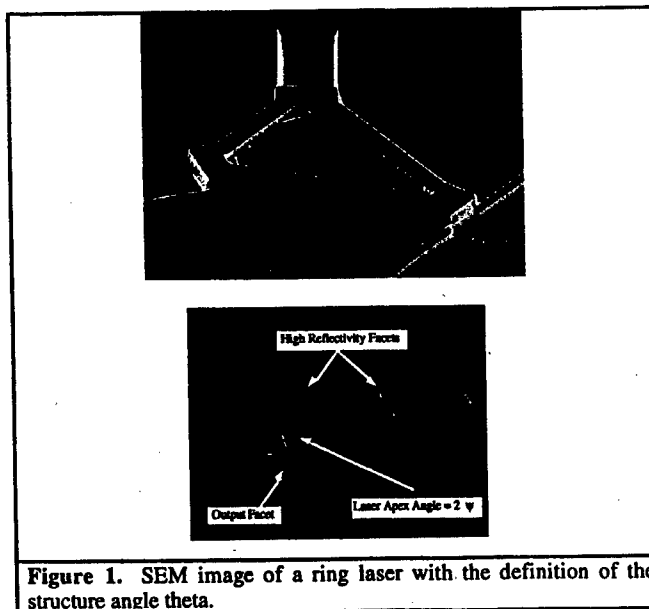


**Figure 1.** SEM image of a ring laser with the definition of the structure angle theta.

Figure 1 shows the triangular ring cavity. The etched facet at the bottom of the picture is the output facet. The laser structure angle theta determines the reflectivity of this facet, and hence the overall cavity Q. The other two mirrors are at large angles to the waveguide, and are nearly totally internally reflecting.

## 2. Theory of Semiconductor Laser Modulation Response

The modulation response of a semiconductor laser can be expressed as the transfer function:

$$H(jw)=(1+jw/wd+(w/wr)^2)^{-1} \quad \text{eq'n 4.8 from thesis} \quad (1)$$

where wr is the relaxation resonance frequency given by

$$wr=\text{sqrt}(Gamma*dg/dn*vg*eta\_i*(I-Ith)/(q*V)) \quad \text{eq'n 4.24 from thesis} \quad (2)$$

where Gamma is the mode overlap fraction, dg/dn is the differential gain, vg is the modal group velocity, eta_i is the internal quantum efficiency, I is the drive current, Ith is the threshold current, q is the electronic charge, and V is the active region volume. The damping frequency wd is given by

$$wd=wr^2/(gamma+1/tau\_e\_prime) \quad \text{eqn. 4.10 from thesis} \quad (3)$$

where tau_e_prime is the effective carrier lifetime and gamma is the damping rate. At moderate drive currents, the relaxation resonance is strong, and the 3dB modulation bandwidth determined from equation (1) is approximately proportional to the resonance frequency wr. At very high drive currents, the 3dB modulation bandwidth asymptotically approaches a constant value. This upper limit is normally expressed as the modulation K-factor, which is the inverse of the maximum modulation frequency:

$$K=4*pi^2/wd=(2*pi)^2/vg*(epsilon/(dg/dn)+1/(alpha\_i+alpha\_m)) \quad \text{eqn 4.17 from thesis} \quad (4)$$

where epsilon is the nonlinear gain saturation coefficient, alpha_i is the internal scatter loss, and alpha_m is the mirror loss. If the differential gain and nonlinear gain saturation are strictly material parameters, then the K-factor will depend on the total cavity mirror reflectivity through the alpha_m term. For the ring lasers, the cavity reflectivity can vary from about 0.1 to 0.7 depending on the choice of structure angle, as shown in Figure 2.
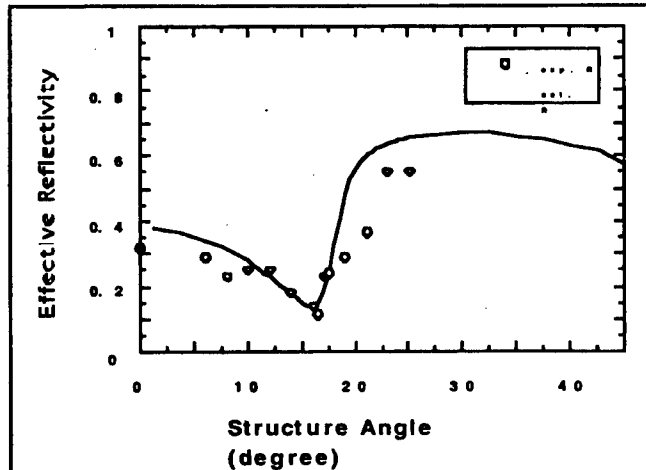


**Figure 2.** Theoretical prediction and experimental verification of dependence of cavity reflectivity on structure angle. Theory from .au [5], data from Liang [1].

At very small angles, the ring approximates a Fabry Perot cavity. At higher structure angles, around 15°, the TE-polarized waveguide mode is near its Brewster angle and hence exits the waveguide with very little reflection, resulting in low cavity reflectivity. At still higher angles, above the critical angle, the cavity reflectivity increases again as the light becomes mostly internally reflected. Over the wide range of cavity reflectivities possible for the ring structure, only about a 20% change in the K-factor is predicted using typical values of differential gain, nonlinear gain saturation, and internal loss for a 600 micron long ring cavity.

For quantum well lasers, the assumption of differential gain independent of the cavity reflectivity is not very accurate. Because the peak gain tends to saturate with increasing current [6], the differential gain will follow a similar dependence on the threshold current density. This effect will be called linear gain saturation. Because lower cavity reflectivity causes higher threshold current which results in lower differential gain, changes in the cavity reflectivity can induce opposing changes to the K-factor due to the mirror loss term and the differential gain. The magnitude of the linear gain saturation will determine which effect dominates.

In many cases, the K-factor is not a good predictor of the practically achievable modulation bandwidth. The K-factor limit can only be reached at rather high drive current levels. Many if not most practical systems will be limited to moderate current levels by catastrophic damage, rapid device degradation, or heat removal concerns. In this situation, the modulation bandwidth will be determined by the relaxation resonance frequency given in equation (2). This expression does not include an explicit mirror loss term. The drive current limited bandwidth is determined primarily by the absolute current level above threshold, the differential gain, and the active region volume. For most quantum well lasers, the active region thickness will be nearly proportional to the mode overlap, so the active region volume and mode overlap dependence of the relaxation frequency becomes a length dependence. A device most useful for OEICs would be able to achieve a high modulation bandwidth at a low current level. Equation (2) shows that such a device would have a low threshold current, high differential gain, and short length.

In order to remove the confounding effects of device and package parasitics, the relative intensity noise spectra can be used to determine the differential gain and K-factor. Following the method presented in [7], the measured RIN is fitted to a curve of the form

$$RIN(f) = (A*f^2 + B) / ((f^2 - f_r^2)^2 + (gamma/2pi)^2 * f^2) \quad \text{eqn 4.22 from thesis} \quad (5)$$

where fr is the relaxation resonance frequency in Hz, gamma is the damping rate, and A and B are bias-dependent, frequency-independent quantities treated as free fitting parameters. At each drive current level, a RIN spectrum is measured and fitted to equation (5), resulting in values for A, B, fr, and gamma. Using these results with equation (2), the differential gain can be determined, and with equations (3) and (4), the K-factor can be determined.


## 3. Experimental Results

### Laser Structure and Fabrication

The lasers were fabricated in an AlGaAs/GaAs GRINSCH structure material with 0.2 micron graded regions and double $In_{0.2}Ga_{0.8}As$ quantum well active region with GaAs barriers. The fabrication process basically followed that presented in [4], with the addition of an n-contact pad on the top side of the wafer to allow on-chip probing with a Cascade coplanar microwave probe. Ring lasers with 600 micron cavity length and varying structure angle were fabricated alongside Fabry Perot lasers with cavity lengths ranging from 100 to 800 microns.
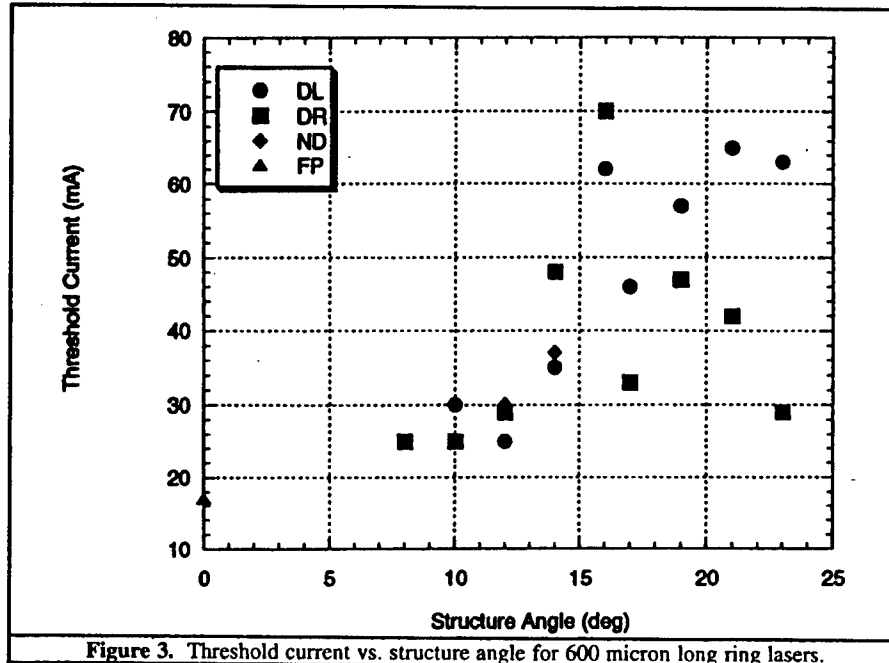
**Figure 3.** Threshold current vs. structure angle for 600 micron long ring lasers.

The threshold currents of the ring lasers are plotted as a function of structure angle in Figure 3. For small angles up through the Brewster angle at 16°, the threshold currents behave as would be expected from the curve in Figure 2. At high angles, the predicted lower threshold currents did not occur. This is attributed to roughness of the etched mirrors, which was worse than in most of our previous work.

## Relative Intensity Noise Spectra

RIN spectra were collected by coupling laser light with lenses through an optical isolator and into a single mode fiber, which was used as input to an HP 71400C Lightwave Signal Analyzer. The lasers were mounted with thermally conductive paste on a temperature controlled stage maintained at 0°C to prevent device degradation during CW operation. Measured noise spectra were do nloaded to a computer for curve fitting.
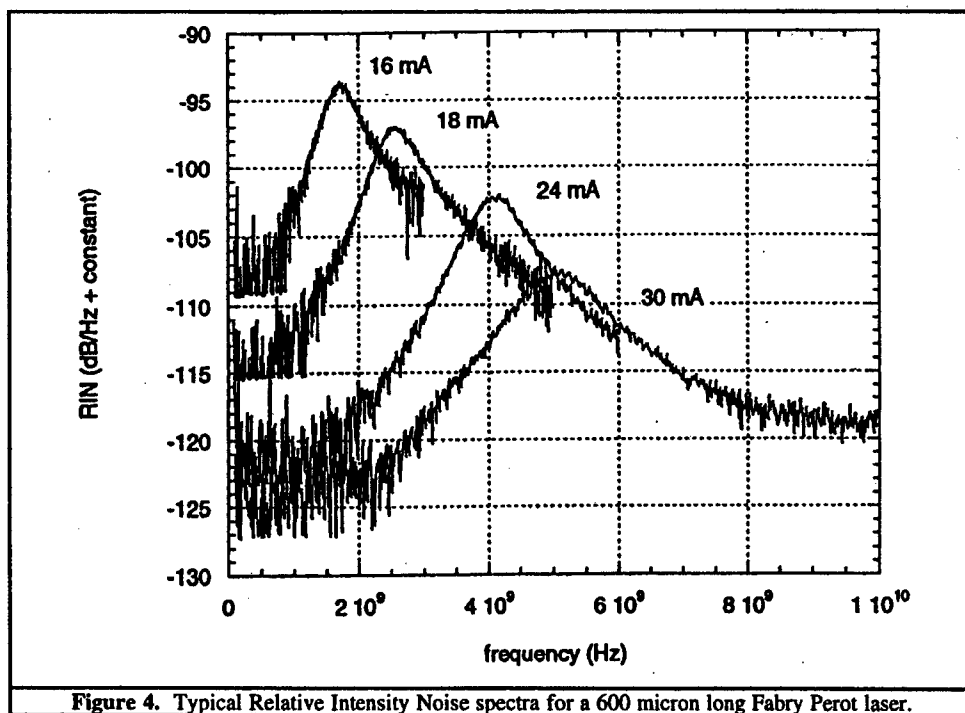
**Figure 4.** Typical Relative Intensity Noise spectra for a 600 micron long Fabry Perot laser.

Typical noise spectra for a 600 micron long Fabry Perot laser are shown in Figure 4 for various drive currents. These spectra were well behaved and easy to accurately fit to equation 5. Values for differential gain, damping rate, and K- factor were extracted as described in the previous section. The maximum intrinsic modulation bandwidth, which is inversely related to the K-factor, is shown in Figure 5 plotted against inverse cavity length, which is proportional to mirror loss for Fabry Perot lasers, and against differential gain. The plots clearly show that the linear gain saturation dependence dominates the K-factor, and the direct mirror loss dependence is negligible in comparison.

A2-5

**Figure 5.** Intrinsic maximum modulation bandwidth for Fabry Perot lasers as extracted from RIN measurements. (a) Maximum modulation bandwidth vs inverse cavity length. (b) Maximum modulation bandwidth vs effective differential gain.

**Figure 6.** Typical RIN spectrum for a ring laser. This example is a 600 micron long, 17° structure angle device.
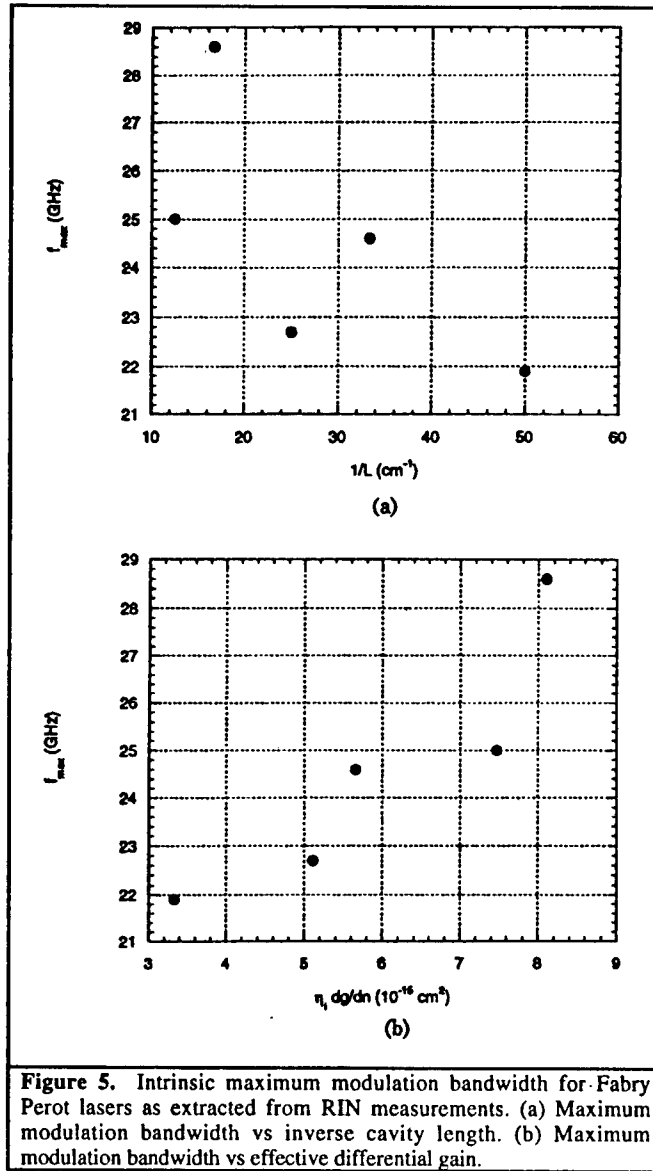
Figure 6 shows a typical RIN spectrum for a ring laser, in this case a 600 micron long cavity with 17° structure angle. The unusual double-peaked shape is immediately obvious. The strength of the lower frequency noise peak varied from barely noticeable to larger than the high frequency noise peak. The low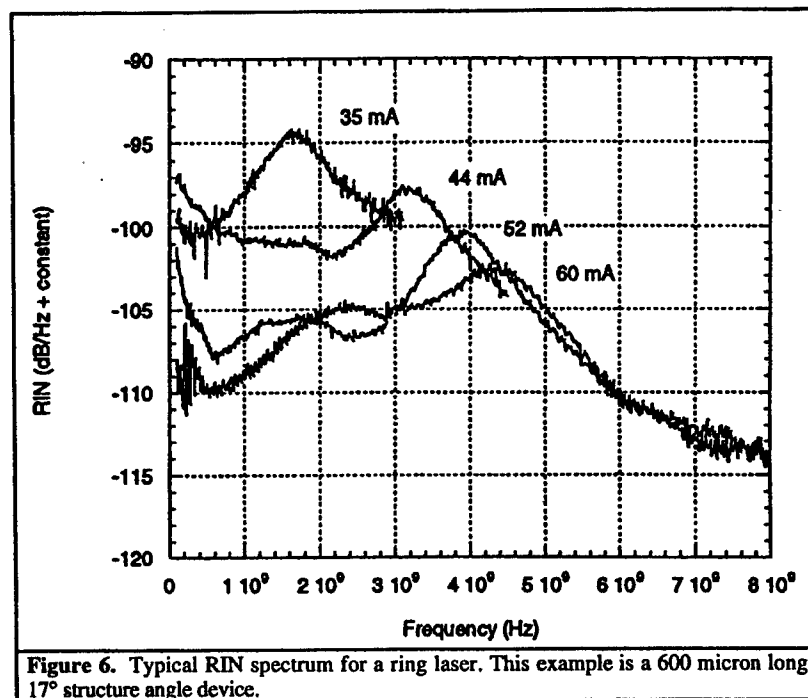 frequency peak was nearly constant in frequency as the drive current was increased, while the higher frequency peak advances in the expected fashion. The exact cause of the additional peak is still under investigation and will not be discussed here, except to note that its presence made accurate determination of the damping rate gamma impossible for the ring lasers. This prevented determination of the K-factor for the ring lasers, but since the relaxation resonance frequency could still be determined with good accuracy, the differential gain could still be determined for the ring lasers. The effective differential gain for both 600 micron ring lasers of varying structure angle and Fabry Perot lasers of varying lengths are shown in Figure 7. The exact dependence of the differential gain on threshold current density is expected to be between $1/\sqrt{(J_{th})}$ for purely radiative recombination and $1/J_{th}$ for a substantial fraction of nonradiative recombination consuming the injected carriers. The empirical good fit to the $1/J_{th}$ dependence shown in Figure 7 indicates a large component of parasitic nonradiative recombination for these devices.

**Figure 7.** Effective differential gain for ring and Fabry Perot lasers, as a function of inverse threshold current density
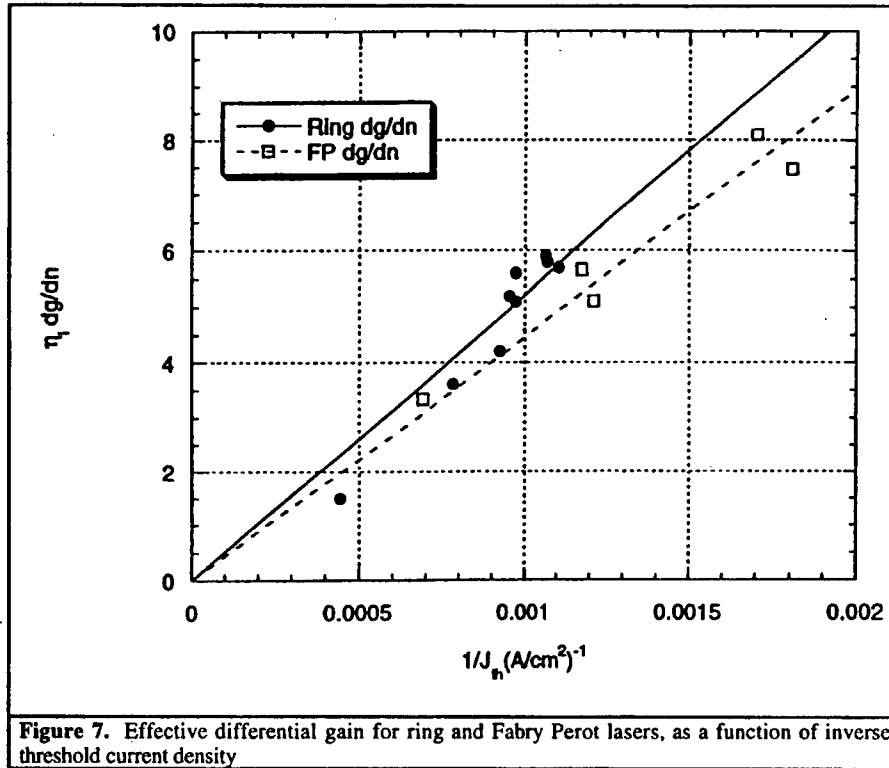
Most importantly, the ring and Fabry Perot lasers both show the same dependence of differential gain on threshold current density. Some of the ring lasers appear to have slightly higher effective differential gain than the Fabry Perot lasers, however, this is believed to be due to distortion of the apparent position of the relaxation resonance peak due to the presence of the enhanced lower frequency noise.

## Direct Modulation Measurements

D⁺rect modulation measurements were performed using an HP8510C Vector Network Analyzer to measure the magnitude of the transmission coefficient S21 and the magnitude and phase of the reflection coefficient S11. The lasers were probed with a Cascade ACP50 coplanar probe tip connected to port 1 of the HP8510. A constant current bias was supplied through the HP8510's bias port, and the HP8510's test set provided the microwave stimulus. The laser light was again collected through an optical isolator into a single mode fiber, which connected to a New Focus Model 1414 photodiode. The photodiode output was connected to port 2 of the HP8510.

A2-8
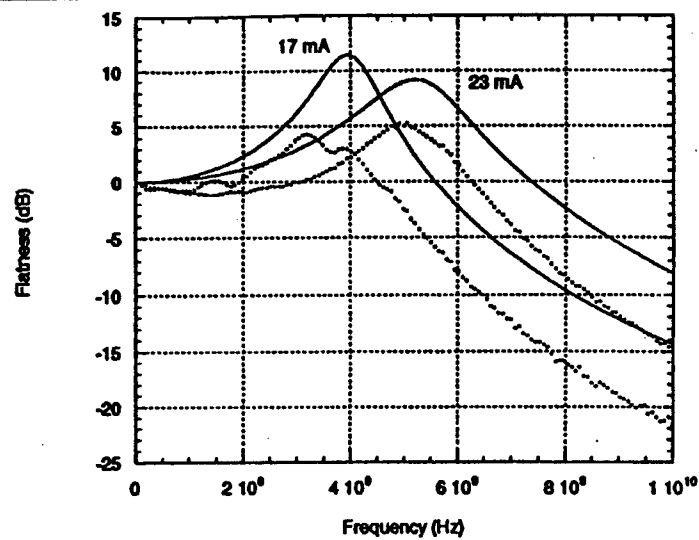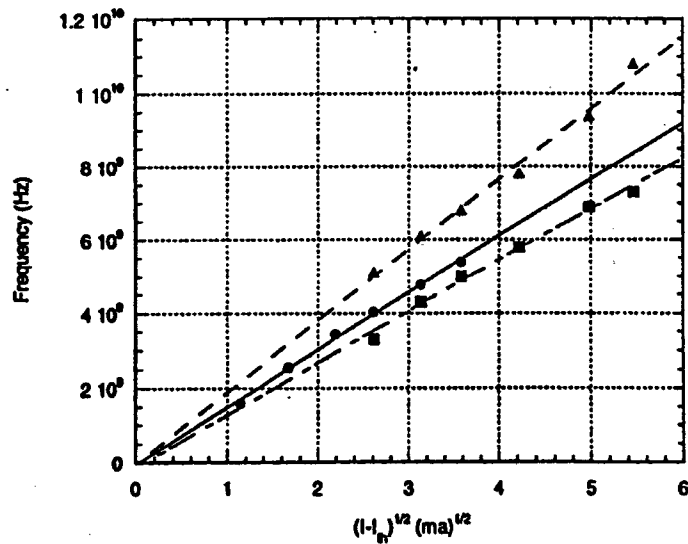
**Figure 8.** Direct modulation properties of a 300 micron long Fabry Perot laser. (a) Measured direct modulation spectrum (points) and spectrum predicted by RIN measurements (solid line). (b) Relaxation frequency from RIN measurements (circles), relaxation frequency from direct modulation measurements (squares), and 3dB direct modulation bandwidth (triangles) as a function of the square root of current in excess of threshold.

A2-9

Figure 8(a) shows the measured direct modulation response (dots) of a 300 micron Fabry Perot laser along with the modulation response predicted by the RIN measurements (solid line). The resonance peak appears at the same frequency in both measurements, but the direct modulation measurement suffers some rolloff due to parasitics which have little effect on the RIN. Figure 8(b) shows another comparison of the RIN and direct modulation measurements. The position of the resonance peak, measured by curve fit for the RIN and by finding the maximum value for the direct modulation, are shown as circles and squares, respectively. The two measurements are in good agreement, with the values of direct modulation appearing at slightly lower frequencies because the resonance peak is superimposed on the parasitic rolloff. The triangles on the plot are the measured 3dB direct modulation bandwidths, which are nearly proportional to the relaxation resonance frequency as predicted by equation (1) for moderate drive levels. The K-factor limit for this device is about 25 GHz, well above the 10 GHz bandwidths shown in the plot.



**Figure 9.** Direct modulation properties of an 8° 600 micron ring laser. (a) Measured direct modulation spectra. (b) Relaxation frequency from RIN measurements (circles) and 3dB modulation bandwidth (triangles) as a function of the square root of current in excess of threshold.
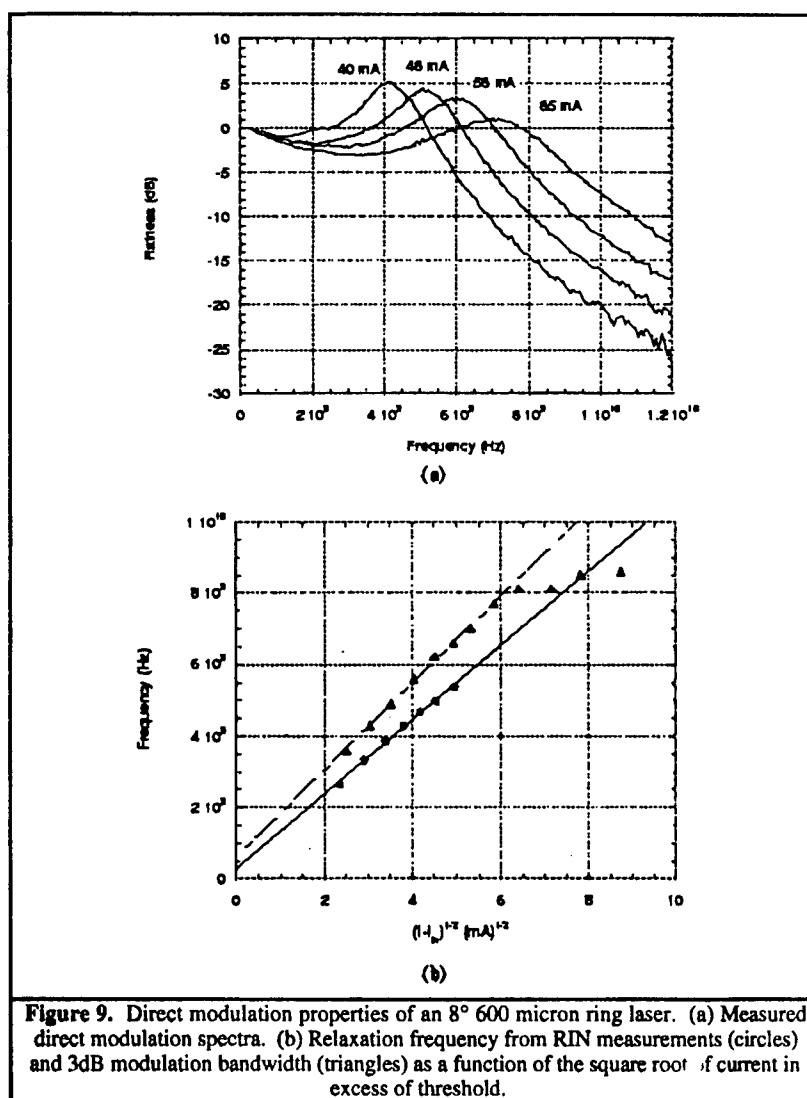
The same information is shown in Figure 9 for a 600 micron ring laser with an 8° structure angle. The RIN measurements could not be used to predict the direct modulation response in this case because the damping rate gamma could not be accurately determined, as discussed earlier. The direct modulation spectra shown, however, do not display the double peak present in the noise spectra. In fact, all of the measured direct modulation spectra exhibited only a single resonance peak, even for lasers for which the second noise peak was particularly strong. The measured 3dB direct modulation bandwidths, shown as triangles in Figure 9(b), are compared to the relaxation resonance frequency, shown as circles. Again, the two are nearly proportional at moderate drive levels. At currents higher than 25mA above threshold and frequencies higher than 8GHz, the proportionality breaks down due to parasitic rolloff.



**Figure 10.** Measured 3dB direct modulation bandwidths as a function of the square root of current in excess of threshold. Open symbols are Fabry Perot lasers: circles 300 microns; squares 400 microns; diamonds 600 microns. Filled symbols are 600 micron ring lasers: circles 8 deg, squares 10deg, diamond 12deg, triangle 14deg, inverted triangle 16deg, plus sign 17deg.
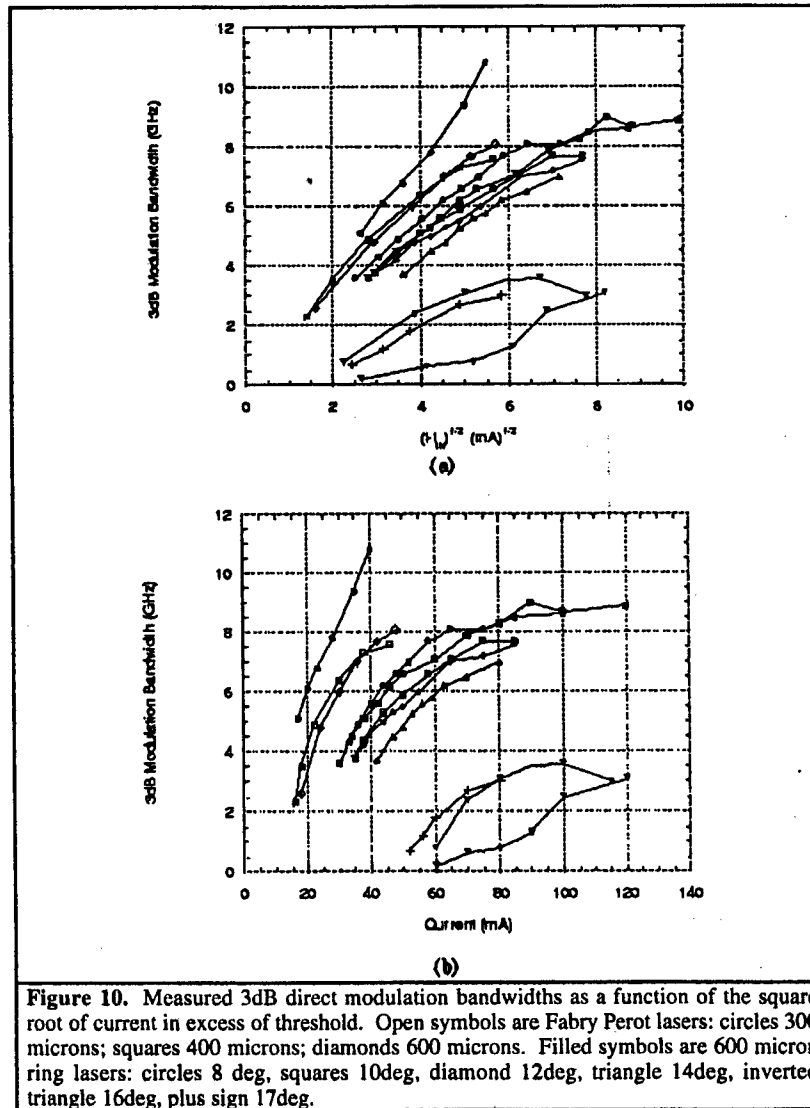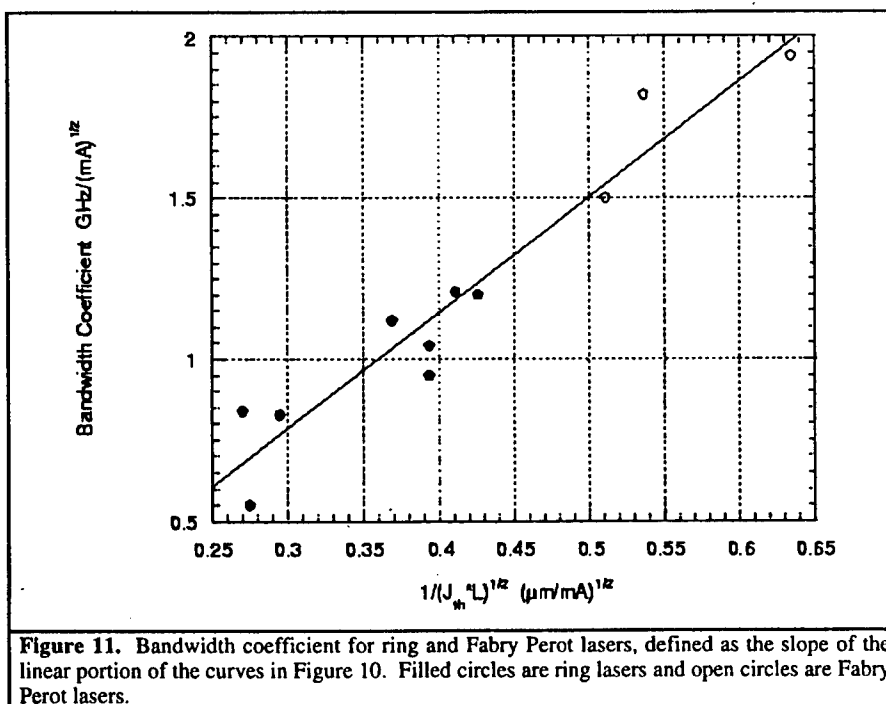
Figure 10 shows the measured 3dB modulation bandwidth as a function of the square root of current in excess of threshold for Fabry Perot lasers of varying lengths and 600 micron long ring lasers of varying structure angle. The steepest slope occurs for the shortest laser, as predicted by equation (2). For the ring lasers, the top curves with the steepest slopes are devices having the smallest structure angles, with increasing structure angle up to the Brewster angle for the devices at the bottom of the plot. As seen in Figure 3, the threshold current increases slowly with structure angle up to about 14°, after which it begins increasing rapidly. Figure 7 shows that this directly impacts the differential gain, which affects the 3dB bandwidth according to equation (2), so the devices with higher thresholds have lower 3dB bandwidths at a given current level.

Also seen in Figure 10 is the deviation from linearity of the bandwidth vs current relation beginning around 20-25 mA above threshold and 6-8 GHz bandwidth for the longer Fabry Perot lasers and the narrow angle ring lasers. The observed nonlinearity is consistent with rolloff from parasitic capacitance rather than the K-factor limit. Above about 100 mA of total current, most devices degraded rapidly and ceased lasing. Although the K-factor predicted bandwidths in the 20-30 GHz range for the Fabry Perot lasers, device degradation prevented observation of bandwidths that high.



**Figure 11.** Bandwidth coefficient for ring and Fabry Perot lasers, defined as the slope of the linear portion of the curves in Figure 10. Filled circles are ring lasers and open circles are Fabry Perot lasers.

The bandwidth coefficient plotted in Figure 11 is the slope of the curves in Figure 10 in the low current regime before the parasitic rolloff began to occur. The coefficient quantifies the amount of current required to achieve a given modulation bandwidth in the range of bandwidths below the K-factor limit. The bandwidth coefficient is expected to be proportional to the factor relating the relaxation frequency to drive current. Equation (2) shows this to be proportional to the square root of differential gain and inversely proportional to the square root of active region volume. The differential gain for these lasers was shown earlier to be inversely proportional to the threshold current density. Since all the lasers share the same waveguide, the active region volume is directly proportional to the length of the laser cavity. The independent variable in Figure 11, then, is proportional to the differential gain divided by the active region volume, and the linear relation with the bandwidth coefficient is exactly as expected. The important feature of this plot is that the Fabry Perot lasers, shown as open circles, and ring lasers, shown as filled circles, both follow the same predicted dependence, indicating that the ring cavity did not have any unexpected effect on the differential gain or modulation bandwidth. The unique feature of the ring structure that this curve illustrates clearly is the ability to create different cavity Q, and consequently different modulation bandwidths, with a constant cavity length, monolithically on the same chip without the use of facet coatings.

**Parasitic Capacitance**

The magnitude of the parasitic capacitance due to the intrinsic diode junction and the large probe pad were estimated by measuring the microwave reflection coefficient of the laser at zero bias. Using the zero bias measurement improved the sensitivity of the measurement to the pad capacitance by minimizing the large capacitance associated with carrier diffusion across the separate confinement region [8] and by eliminating the differential junction resistance as a fitting parameter. The measured load impedances were fitted to a simple circuit model including capacitance of the junction, capacitance of the probe pad, and the contact resistance. The fit was performed for varying sizes of device simultaneously . The resulting values for the parasitics were pad capacitance and junction capacitance of 10 nF/cm^2 each and series contact resistance of 0.22 milliohm*cm^2. The pad capacitance was consistent with the thickness of the silicon dioxide insulating the pad from the semiconductor. The junction capacitance was somewhat higher than expected at zero bias, but could be explained by current spreading beyond the shallow-etched waveguide ridge. The measured capacitance is also consistent with the observed parasitic rolloff beginning around 3GHz in Figure 8.

## 4. Conclusions

We have presented the first measurements of the modulation properties of etched facet waveguide diode ring lasers, a novel laser structure well suited to the requirements of monolithic OEICs. Relative Intensity Noise spectra and direct modulation spectra were measured to study the modulation properties. Both the ring lasers and standard Fabry Perot lasers fabricated on the same chip were found to have modulation bandwidths determined by the differential gain and cavity length in the same way. The differential gain was completely determined by the threshold current density, and variations in the differential gain overwhelmed the relatively weak direct photon lifetime dependence of the modulation K-factor. The capacitance of the large contact pad filling the center of the ring was measured and was found to be consistent with the thickness of the dielectric isolating the pad from the semiconductor.

The ring lasers were found to exhibit a structure angle dependence of the modulation bandwidth which was consistent with the observed and predicted cavity Q. The varying cavity Q is achievable at a constant cavity length without the use of facet coatings. The ability to create high cavity Q will

allow the creation of very short lasers with reasonable threshold current density. The relatively long photon lifetime of such a device would have only a minor effect on the K-factor bandwidth limit, but the short length would provide a high bandwidth coefficient, allowing the device to reach bandwidths below the K-factor limit at low drive current levels.

## REFERENCES:

[1]    Liang, J., and Ballantyne, J. M., "Monolithic Ring Lasers for Low-Noise Optical Signal Distribution," Proceedings SPIE vol. 2155, Optoelectronic Signal Processing for Phased Array Antennas IV, pp. 142-49, 1994.

[2]    Ji, C., Leary, M., and Ballantyne, J. M., "Long Wavelength Triangular Ring Laser," IEEE Photonics Technology Letters, 9 (11) pp. 1469-71, November 1997.

[3]    Liang, J., Lau, S., Leary, M., and Ballantyne, J. M., "Unidirectional Operation of Waveguide Diode Ring Lasers," Appl. Phys. Lett. 70 (10) pp. 1192-94,1997.

[4]    Liang, J., and Ballantyne, J. M., "Self Aligned Dry Etching Process for Waveguide Diode Ring Lasers," Journ. Vac. Sci. Tech. B., 12 (5) pp. 2929-32,1994.

[5]    Liang, J., Lau, S., and Ballantyne, J. M., "Unique Aspects of Waveguide Diode Ring Lasers," Proceedings of the Lasers and Electro-Optics Society Annual Meeting 1994, Vol. 2, p. 393, paper SL10.5, 1994.

[6]    McIlroy, Kurobe, and Uematsu, "Analysis and Application of Theoretical Gain Curves to the Design of Multi-Quantum Well Lasers," IEEE Journ. Quantum Elect., QE-21 (12) pp. 1958-63, 1985.

[7]    Ralston, Weisser, Esquivias, Larkins, Rosenzweig, Tasker, and Fleissner, "Control of Differential Gain, Nonlinear Gain, and Damping Factor for High Speed Application of GaAs-Based MQW Lasers," IEEE Journ. of Quantum Electronics, 29 (6) pp. 1648-59, 1993.

[8]    Weisser, Esquivias, Tasker, Ralston, and Rosenzweig, "Impedance, Modulation Response, and Equivalent Circuit of Ultra-High Speed InGaAs/GaAs MQW Lasers with p-Doping," IEEE Photon. Tech. Lett. 6 (7) pp. 782- 85, 1994.

## Visible Electroluminescence (630nm) from Direct Bandgap GaInP Quantum Dots Grown on Transparent GaP Substrates

Jong-Won Lee, A.T. Schremer, J.R. Shealy, J.M. Ballantyne
School of Electrical Engineering, Cornell University
Phillips Hall, Ithaca, NY 14853

### Summary

Not much progress has been made with optoelectronic devices on GaP and Si substrates /owing to the lack of light emitting materials that can be epitaxially grown on these substrates with a low defect density. All currently available light emitting semiconductor compounds have lattice constants different from GaP and Si lattice constants, and therefore no thin films of useful thicknesses can be grown defect-free. Recently a new technique of embedding pockets of strained material into a host matrix without dislocating the crystal lattice has received much attention: strain-induced self-assembled quantum dots. Indeed, InAs/GaAs quantum dots have been successfully used as the active region of semiconductor laser devices with excellent device characteristics.[1] We used a similar approach to induce formation of light-emitting GaInP quantum dots on GaP substrates.[2,3] In this presentation, we report fabrication of light-emitting diodes (LEDs) with GaInP quantum dots as the active region.

The layer structure of the LED device is shown in Figure 1. The LED heterostructures were grown at 650°C in 76 torr $H_2$ ambient. For the backside contacts, Ni/Ge/Au was evaporated and annealed. On the frontsides of the wafers, Ti/Pt/Au 500μm diameter circular contacts were evaporated through a shadow mask. Finished chips were packaged onto off-the-shelf chip-packages for testing. The emitted light was collected from the cleaved facets of the chips.

When examined under a microscope, it was found that the underside of the top contact was not uniformly illuminated: spots of bright regions could be seen. The spots constituted only a small fraction (<5%) of the device area. This is probably because Ti/Pt/Au does not make a good contact with GaP. The device characteristics of the LEDs at room temperature are shown in Figure 2. The small output power is attributed to the aforementioned metal contact problem and the inefficient light extraction geometry. The electroluminescence spectrum has similar features as the photoluminescence spectrum (Figure 3). The emission intensity vs. the sample temperature of electroluminescence deviated from that of photoluminescence (Figure 4): the curve is temperature-shifted by ~50°. The probable cause is device heating, which made the temperature of the active region higher than the measured sample holder temperature. The reduction of the PL intensity at temperatures below 140K is due to charge carrier condensation into the wetting layer GaInP.[3]

A successful demonstration of simple GaInP/GaP quantum dot LEDs suggests potentials for more advanced optoelectronic devices on GaP substrates and possibly on Si substrates.

### References

1. F. Heinrichadorff, A. Krost, M.-H. Mao, N. Kirstaedter, A.O. Kosogov, P. Werner, D. Bimberg, Eight Biennial Workshop on Organometallic Vapor Phase Epitaxy, Dana Point, CA, Apr. 13 - Apr. 17 (1997).
2. J.-W. Lee, A. Schremer, D. Fekete, J. Ballantyne, to be published in Journal of Electronic Materials.
3. J.-W. Lee, A.T. Schremer, D. Fekete, J.M. Ballantyne, Appl. Phys. Lett. 69 (1997) p4236.

Light
emission

Photodetector
(not to scale)

Cleaved
facet

Ti/Pt/Au contact
300Å p+ GaP (Zn)

5000Å p GaP (Zn)

1000Å undoped GaP
GaInP quantum dots
1000Å undoped GaP
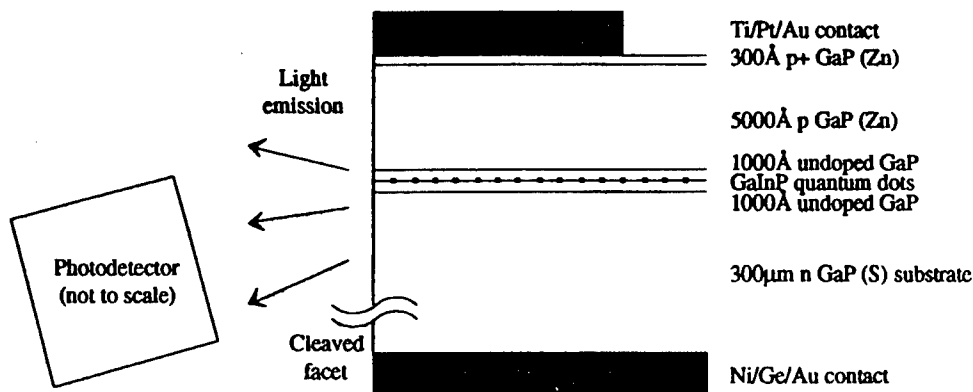
300μm n GaP (S) substrate

Ni/Ge/Au contact

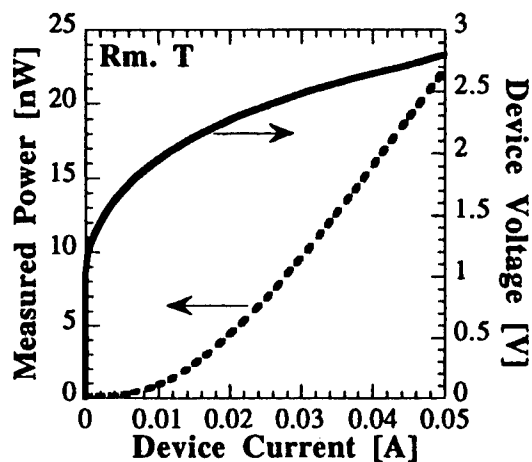Figure 1. The LED device layer structure and the measurement arrangement.



Figure 2. P-I-V curve of the LED device at room temperature.
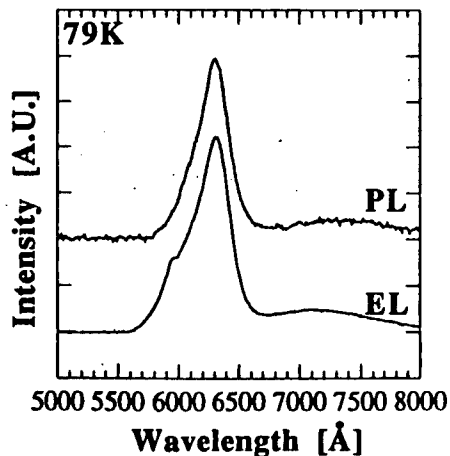When cooled to 100K, the light intensity increased by 30x.
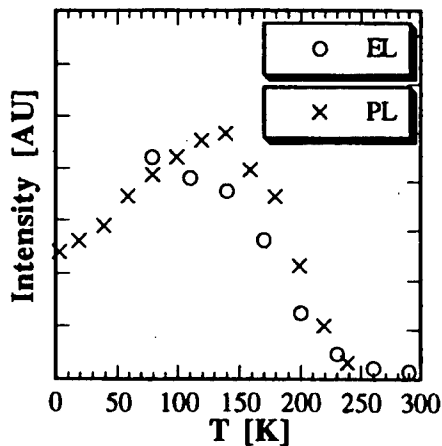


Figure 3. Comparison between PL and EL spectra.



Figure 4. Maximum intensity vs. T.

A3-2

# *MISSION*
## *OF*
### *AFRL/INFORMATION DIRECTORATE (IF)*

The advancement and application of information systems science and technology for aerospace command and control and its transition to air, space, and ground systems to meet customer needs in the areas of Global Awareness, Dynamic Planning and Execution, and Global Information Exchange is the focus of this AFRL organization. The directorate's areas of investigation include a broad spectrum of information and fusion, communication, collaborative environment and modeling and simulation, defensive information warfare, and intelligent information systems technologies.